POLITECNICO DI TORINO
Repository ISTITUZIONALE

Arctic Weather Satellite Sensitivity to Supercooled Liquid Water in Snowfall Conditions

Original
Arctic Weather Satellite Sensitivity to Supercooled Liquid Water in Snowfall Conditions / Camplani, A., Sanò, P., Casella, D., Panegrossi, G., Battaglia, A.. - In: REMOTE SENSING. - ISSN 2072-4292. - 16:22(2024). [10.3390/rs16224164]

Availability:
This version is available at: 11583/2995843 since: 2024-12-23T10:35:35Z

Publisher:
MDPI

Published
DOI:10.3390/rs16224164

Terms of use:

This article is made available under terms and conditions as specified in the corresponding bibliographic description in the repository

Publisher copyright

(Article begins on next page)

26 November 2026

remote sensing

MDPI

Article

Arctic Weather Satellite Sensitivity to Supercooled Liquid Water in Snowfall Conditions

Andrea Camplani [1], Paolo Sanò [1], Daniele Casella [1,*], Giulia Panegrossi [1] and Alessandro Battaglia [2,3,4]

[1] National Research Council of Italy, Institute of Atmospheric Sciences and Climate (CNR-ISAC), 00133 Rome, Italy; andrea.camplani@artov.isac.cnr.it (A.C.); p.sano@isac.cnr.it (P.S.); g.panegrossi@isac.cnr.it (G.P.)
[2] National Centre for Earth Observation, University of Leicester, Leicester LE1 7RH, UK; alessandro.battaglia@polito.it
[3] Department of Environment, Land and Infrastructure Engineering (DIATI), Politecnico di Torino, 10129 Turin, Italy
[4] Department of Physics and Astronomy, University of Leicester, Leicester LE1 7RH, UK
* Correspondence: daniele.casella@artov.isac.cnr.it

Abstract: The aim of this study is to highlight the issue of missed supercooled liquid water (SLW) detection in the current radar/lidar derived products and to investigate the potential of the combined use of the EarthCARE mission and the Arctic Weather Satellite (AWS)—Microwave Radiometer (MWR) observations to fill this observational gap and to improve snowfall retrieval capabilities. The presence of SLW layers, which is typical of snowing clouds at high latitudes, represents a significant challenge for snowfall retrieval based on passive microwave (PMW) observations. The strong emission effect of SLW has the potential to mask the snowflake scattering signal in the high-frequency channels (>90 GHz) exploited for snowfall retrieval, while the detection capability of the combined radar/lidar SLW product—which is currently used as reference for the PMW-based snowfall retrieval algorithm—is limited to the cloud top due to SLW signal attenuation. In this context, EarthCARE, which is equipped with both a radar and a lidar, and the AWS-MWR, whose channels cover a range from 50 GHz to 325.15 GHz, offer a unique opportunity to improve both SLW detection and snowfall retrieval. In the current study, a case study is analyzed by comparing available PMW observations with AWS-MWR simulated signals for different scenarios of SLW layers, and an extensive comparison of the CloudSat brightness temperature (TB) product with the corresponding simulated signal is carried out. Simulated TBs are obtained from a radiative transfer model applied to cloud and precipitation profiles derived from the algorithm developed for the EarthCARE mission (CAPTIVATE). Different single scattering models are considered. This analysis highlights the missed detection of SLW layers embedded by the radar/lidar product and the sensitivity of AWS-MWR channels to SLW. Moreover, the new AWS 325.15 GHz channels are very sensitive to snowflakes in the atmosphere, and unaffected by SLW. Therefore, their combination with EarthCARE radar/lidar measurements can be exploited to both improve snowfall retrieval capabilities and to constrain snowfall microphysical properties.

Keywords: AWS; supercooled liquid water; microwave remote sensing; snowfall retrieval

check for updates

Citation: Camplani, A.; Sanò, P.; Casella, D.; Panegrossi, G.; Battaglia, A. Arctic Weather Satellite Sensitivity to Supercooled Liquid Water in Snowfall Conditions. *Remote Sens.* **2024**, *16*, 4164. https://doi.org/10.3390/rs16224164

Academic Editor: Alexander Kokhanovsky

Received: 25 September 2024
Revised: 30 October 2024
Accepted: 1 November 2024
Published: 8 November 2024

Copyright: © 2024 by the authors. Licensee MDPI, Basel, Switzerland. This article is an open access article distributed under the terms and conditions of the Creative Commons Attribution (CC BY) license (https://creativecommons.org/licenses/by/4.0/).

1. Introduction

Snow is an essential variable in the Earth climate system. High-latitude regions, in particular, where snow plays a key role in the water and energy cycle, are experiencing significant changes linked to climate change. However, snowfall retrieval represents a challenging question in the atmospheric science field. Ground-based instruments, such as snow gauges and weather radars, provide only local areal measurements; moreover, in most of the regions where snowfall is predominant, weather observation networks are very

scarce or totally absent. Therefore, the refinement of satellite-based methods for snowfall retrieval is necessary for global monitoring of snowfall [1–4].

Spaceborne microwave (MW) sensors have been largely used to detect and extract quantitative information on snowfall, thanks to their ability to probe within clouds. The polar orbiting, W-band high sensitivity Cloud Profiling Radar (CPR) has been operating on the NASA CloudSat mission since 2006 [5], and is now available on the recently launched ESA/JAXA Earth Cloud Aerosol and Radiation Explorer (EarthCARE) mission [6]. Moreover, it is foreseen for the WIVERN mission, currently in Phase A in the ESA Earth Explorer Program, which would be the first space-based mission providing in-cloud winds, along with high-resolution reflectivity profiles of rain, snow, and ice water [7]. CPR is considered the most suitable sensor for snowfall monitoring at higher latitudes (as demonstrated in several studies, e.g., [8,9]) typically characterized by light/moderate intensity [10]. CloudSat has provided unprecedented datasets for the study of clouds and global snowfall up to 82° latitude. It is worth noting that CPR W-band reflectivity tends to saturate in heavier and deeper snowfall events due to non-Rayleigh effects [11,12], may be affected by attenuation because of the presence of supercooled liquid water (SLW) [13], and is affected by ground clutter [9,14–16], with significant impact on the climatology of shallow snowfall events [8]. Moreover, CloudSat CPR has worked in a day-only operation mode since 2011 [17]. In spite of these limitations, the CPR has shown superior capabilities with respect to the other spaceborne instruments, including the Ku/Ka-band scanning Dual-frequency Precipitation Radar (DPR) on board the Global Precipitation Measurement (GPM) mission Core Observatory [18]. The DPR lower sensitivity does not allow light snowfall occurrence to be properly accounted for and quantified [19], and its limited latitudinal coverage (up to 65°N/S) does not allow for a global snowfall climatology. A quality assessment of several satellite-based snowfall products over the ground-based radar network of the continental U. S. showed that CloudSat-CPR gives the best detection statistical scores [11]. However, CPR is nadir-looking and has a limited swath (1.5 km), and does not provide the needed coverage for frequent monitoring of snowfall. If selected, WIVERN will remedy this drawback [20].

Therefore, satellite snowfall monitoring is mainly based on the observations of passive microwave (PMW) sensors onboard Low Earth Orbit (LEO) satellites [21,22] which offer better coverage, thanks to an increasing number of platforms and wide swaths, and good sensitivity to snowfall, as demonstrated by several studies [11,23–29]. The snowfall retrieval is typically based on the ability to interpret the snowfall scattering signature in the high-frequency channels (>90 GHz), which respond more effectively to ice microphysics and are less prone to surface effects than low-frequency channels, and to distinguish it from the clear-sky (surface and atmosphere) contribution (e.g., [30,31]). However, several factors make the PMW snowfall signal ambiguous and the relationship between multi-channel measurements and surface snowfall intensity highly non-linear, especially in extremely cold/dry environmental conditions [4]: the snowfall scattering signal is relatively weak (e.g., [32]), it is highly dependent on the complex microphysical properties of snowflakes (e.g., [24,33,34]), and it can be contaminated by the extremely variable background surface emissivity [31,35–37] and by the presence of SLW [1,38,39]. Moreover, recent studies based on the use of coincident active and passive MW measurements [40] have demonstrated the complex interconnection between all these factors on the PMW multi-channel signature [26,27,37]. It is worth noting that these studies are affected by the intrinsic limitations of the active sensors used as reference, not only to quantify snowfall (mentioned above for CPR and DPR) but also to detect SLW.

The presence of SLW layers is due to the fact that cloud droplets can remain in a metastable liquid condition down to about −40 °C. Below 0 °C, cloud particle populations can consist of a mixture of ice particles and liquid droplets [41]. These mixed-phase clouds are characterized by complex structures both vertically and horizontally [42]. In general, very little SLW is expected because the ice crystals that form in this temperature range will grow at the expense of liquid droplets. However, SLW is often observed at negative temperatures above −20 °C at all latitudes. In addition, recent observations performed

over the Antarctic region have revealed SLW layers with temperature between −20 and −30 °C and liquid water path (LWP) between 0.002 and 0.20 kg m^{-2}. Such layers can have a significant impact on the upwelling microwave radiation [43].

The impact of SLW layers on the PMW upwelling radiation, affecting the snowfall signature, represents one of the most important challenges in snowfall retrieval. Radiometrically, cloud liquid water absorbs and emits measurable microwave energy, generally causing brightness temperature (TB) warming; thus, it can mask the possible ice scattering signature generated by snowfall (TB cooling) [44]. SLW layers are often found in snowing clouds: Wang et al., 2013 [44] reported a frequency of occurrence exceeding >70% over the ice-free ocean, while Battaglia and Delanoë, 2013 [45] found occurrences of 57% and 33% over sea and land. This SLW impact on the PMW signal varies with frequency: at low frequencies (30–50 GHz), this emission signal (TB warming) dominates over the snow particle scattering signal (TB cooling), while between 89 and 94 GHz, the decrease of TB due to snowflake scattering and its increase due to cloud liquid water are comparable; at higher frequencies (>150 GHz), the ice scattering signature dominates more and more. However, the relative influence of the snowflake scattering signature and SLW emission signal is highly dependent on the environmental conditions (mainly the atmospheric moisture) and on the SLW layer height [44].

Currently, SLW layers are detected from satellites by combining lidar and radar observations. Lidar and radar have complementary properties: lidar signals are sensitive to optically thin clouds, such as supercooled water clouds, which are characterized by large numbers of small liquid water droplets, but are rapidly attenuated in optically thick clouds, whereas radar signals are able to penetrate even optically thick clouds, such as ice clouds which are characterized by larger particles, but are less sensitive to optically thin clouds composed of small particles [45–47]. However, the combined radar–lidar product presents some limitations. In particular, the strong extinction of the lidar in a SLW layer precludes detection of any lower liquid layer; moreover, the lidar signal can also be extinguished closer to the surface because of optically thick ice clouds above [48]. On the other hand, PMW observations are sensitive to SLW layers both at the top and embedded in the clouds. Battaglia and Panegrossi, 2020 [13] demonstrated that including the CPR radiometric mode (at 94 GHz) could be very useful for improving the detection of SLW embedded in clouds over ice-free ocean. However, at 94 GHz, the SLW absorption/emission and the snow scattering can partially cancel out the upwelling radiation. Since the different PMW frequencies react differently to the different hydrometeor combinations, multi-channel PMW measurements are the way forward to fully disentangle the two contributions in different snowfall regimes.

Over the last 6 years, PMW machine learning-based algorithms exploiting global observational datasets built from passive and active microwave spaceborne sensors have been demonstrated to be very suitable for global snowfall detection and retrieval [11,49–55] In particular, the Snow retrievaL ALgorithm fOr gMi (SLALOM, [52,53]) for the GPM Microwave Imager and the Snow retrievaL ALgorithm fOr gpM—Cross Track (SLALOM-CT, [54]) for the operational cross-track scanning ATMS onboard JPSS satellite series are trained on CloudSat CPR snowfall measurements and include SLW detection modules. These modules use the CPR-CALIOP DARDAR product [56] as reference. As in most lidar/radar coupled systems, DARDAR detects the SLW near the cloud top while it misses most of SLW embedded in the cloud due to lidar attenuation [52]. Therefore, also in SLALOM and SLALOM-CT, the SLW detection is limited to the occurrences at the cloud top. However, as reported by Mroz et al., 2021 [11], the ability to detect SLW has a positive impact on the accuracy of SLALOM snowfall estimates compared to other PMW products.

The recent launch of the EarthCARE mission, and the availability of multi-channel MW radiometers on board polar orbiting satellites equipped with a large frequency range offer new opportunities both to retrieve the presence of SLW layers and to improve snowfall detection and quantification, especially at higher latitudes. In particular, the recent launch of the Arctic Weather Satellite (AWS) mission (on 16 August 2024), a dedicated mission for

monitoring the Arctic weather, represents a very interesting opportunity to improve both SLW layer and snowfall retrieval. The AWS is equipped with the Microwave Radiometer (MWR), whose channels cover a range from 50 GHz to 325.15 GHz, useful both to retrieve the presence of SLW layers and to improve snowfall detection and quantification. It is therefore important to assess the potential of the AWS-MWR for snowfall retrieval at high latitudes and to investigate the possibility to develop a Machine Learning (ML) based algorithm similar to the SLALOM-CT [54] based on the synergic exploitation of AWS capabilities and the recently launched EarthCARE mission. The AWS will be the forerunner of the potential EUMETSAT Polar System Sterna (EPS-Sterna), itself conceived as a constellation of small (120 kg) polar-orbiting satellites, each carrying a single microwave radiometer providing frequent coverage of the Earth and full coverage of the polar zones with no gaps. EPS-Sterna would complement the MetOp series, as well as the US NOAA's JPSS, by providing more frequent observations, mainly for temperature and humidity sounding. However, thanks to its unprecedented coverage, the AWS constellation offers a unique opportunity for enhancing and improving precipitation monitoring at high latitudes.

The objectives of this study are:

1. Highlight the issue of missed SLW detection in the CAPTIVATE retrieval which will represent the backbone algorithm for the synergistic EarthCARE cloud products and assess the potential using of the 94 GHz radiometric mode;
2. Show the sensitivity of multi-channel AWS measurements to SLW properties in snowfall conditions;
3. Demonstrate the potential of the use of the 325.15 GHz channels to disentangle the contribution of SLW and snowfall to the measured TB.

2. Instruments and Methods

This study is based on the analysis of a 7-day dataset (1 January 2007–7 January 2007) of 49 A-Train CloudSat/CALIPSO complete orbit observations. Cloud and precipitation vertical profiles from combined Cloud Profiling Radar (CPR) and Cloud-Aerosol Lidar with Orthogonal Polarization (CALIOP) observations are derived by applying the Cloud, Aerosol, and Precipitation from mulTiple Instruments using a VAriational TEchnique (CAPTIVATE) algorithm which will be implemented in the EarthCARE mission (ACM-CAP product [57]). These profiles are used in radiative transfer model (RTM) simulations to derive multi-channel brightness temperatures (TBs) to be compared with PMW measurements from existing sensors and to obtain a synthetic AWS-MWR dataset.

In the next sections, the characteristics of the active and passive sensors used in the study and each component of the RTM simulations are described.

2.1. The Cloud Profiling Radar and the CALIPSO Lidar

The CPR is a 94 GHz nadir-looking radar on board CloudSat. CloudSat was launched on 28 April 2006 and operated until December 2023; the W-band CPR operations began on 2 June 2006. CPR has acquired the first-ever continuous global time series of vertical cloud structures and vertical profiles of cloud liquid and ice water content with a 485 m vertical resolution. The 3 dB footprint of the antenna field on view spans 1.4 km [5]. CALIPSO Cloud-Aerosol Lidar with Orthogonal Polarization (CALIOP) is a nadir-viewing, two-wavelength (532 and 1064 nm), polarization-sensitive lidar [58]. It is the first polarization lidar in orbit and the first satellite lidar to provide long-term continuous measurements. Both CloudSat and CALIPSO fly as part of the A-train constellation of satellites, offering a variety of measurement synergies. They have provided multiyear datasets of global aerosol and cloud profiles [59]. CPR and CALIOP observations have been used as input to the CAPTIVATE algorithm to generate microphysics profiles, including SLW layers (see Section 2.4).

The 94 GHz CloudSat TB product is very useful for checking the consistency of the simulations and their sensitivity to the presence of SLW. The TB is calculated from the radiometric measurement obtained by processing the noise floor data contained in the

1B-CPR standard data product. The noise floor is first defined starting from cloud mask and further refined to use only range bins that have no contamination from cloud or surface backscatter. All range bins selected in this way are averaged to obtain a single-profile estimate of background power. The temperature-dependent contributions from the instrument are then removed from the single-profile estimates [60]. Since CloudSat was not designed to act as a radiometer, careful calibration efforts were necessary to translate the received power into a physical TB [61]. This calibration was carried out using carefully screened cloud-free pixels over well-characterized ocean surfaces in conjunction with radiative transfer modeling to translate the AMSR-E TB to the CloudSat frequency and viewing geometry [61]. However, this procedure may be affected by a residual bias [13]. Despite these limitations, the use of the 2B-94TB product has been very useful to obtain a one-to-one comparison between TBs obtained from the CPR measurements and the TBs simulated based on the CAPTIVATE retrievals. However, the limitations of the 2B-94TB product described above, and the fact that it is based on a single frequency, has motivated us to extend the comparison also to observations from available cross-track scanning radiometers, which provide multi-channel measurements similar to AWS.

2.2. The CAPTIVATE Algorithm

CAPTIVATE [62,63] is a synergistic retrieval algorithm for vertically-pointing radars, lidars, and radiometers. It was designed for the instruments onboard the EarthCARE mission. CAPTIVATE exploits the complementary properties of the various sensors to simultaneously retrieve all classes of hydrometeors and aerosols in each profile, and takes account of measurement errors and physical assumptions to report the uncertainties associated with all retrieved quantities for interpretation by users and downstream products [57]. The algorithm is based on an optimal estimator approach. First, a target classification is performed to identify the constituents of each volume (ice, liquid cloud, rain, melting layer, and aerosols). Then, a state vector is constructed, comprising the parameters describing all constituents previously identified in the volume. The state vector is used as input to a forward model to simulate the observations made by each instrument (lidar, radar, and radiometer). The optimal estimate is the state vector that minimizes the cost function between the instrument observations and the forward model output. It is important to underline that the CAPTIVATE algorithm treats all ice hydrometeors that may be present in each bin (e.g., cloud ice, snowflakes, aggregates) as one unique category; as in the CPR measurements, it is not possible to distinguish between the contribution from cloud ice and from precipitating hydrometeors. Therefore, the retrieved IWC refers to all ice/snow hydrometeors found in each bin. For SLW layers, their cloud tops are identified by CALIOP whereas their corresponding liquid water content (LWC) is partly constrained by the MODIS visible radiances. This retrieval has limitations (see [45]), such as the missed detection of embedded SLW layers in deep clouds.

In this work, CAPTIVATE was applied to the observations collected by the CloudSat CPR, the CALIPSO CALIOP, and the MODIS radiometer, all in the same A-Train constellation, for hundreds of orbits [64] in order to obtain cloud and precipitation profiles. Ice Water Content (IWC), Rain Water Content (RWC), and Liquid Water Content (LWC) profiles, obtained by applying CAPTIVATE, were used as input to the RTM. These products are characterized by the CPR horizontal resolution (1.4 km) and a 60 m vertical resolution. A filter was applied to the data to delete outliers. In particular, values higher than the 99th percentile of each variable (IWC, RWC, and LWC) were replaced with the mean values between the nearest four values in the profile.

2.3. The Radiative Transfer Model

The RTM uses the 2-stream Eddington approximation in a plane parallel atmosphere [65,66], widely used for microwave radiation (e.g., [67]). The water vapor and other gas absorption properties were derived by the Rosenkranz model [68]. Temperature and humidity profiles were obtained from the CPR ECMWF-AUX product where

the atmospheric state variables forecasted by the ECMWF model are associated with each CloudSat CPR bin (the product is described by Ref. [69]). The ocean surface emissivity model is TESSEM [70]; two input parameters (wind speed and sea surface temperature) were extracted from the ECMWF-AUX product while the salinity was fixed to 35 g kg^{-1}. In the RT model, the radiative properties of liquid water are obtained from Mie theory; the refractive index used is the one described in [71,72]. The ice hydrometeor scattering was derived from Rayleigh Gans theory [57,73–76]. In order to produce different scattering models, different mass–size relationships were used, following the study of Tridon et al., 2019 [77]. The nomenclature used in this paper is similar to that of the reference (see information about microphysics and scattering models in Table 1). It is important to note that among the assumptions summarized in Table 1, only the one called "captivate" is consistent with the assumptions made in the retrieval scheme. It is also important to underline that the same scattering properties have been applied to the whole ice profiles, because CAPTIVATE does not distinguish between different types of solid hydrometeors (e.g., cloud ice, precipitating snowflakes).

Table 1. Nomenclature and references of the different scattering models. The coefficient for the mass–size relationship $m = \alpha D^{\beta}$ in SI units are also listed in the last two columns.

Scattering Model	Microphysics	Reference	α	β
leinonen A0	simultaneous aggregation and riming—LWP = 0 kg m^{-2}	Leinonen & Szyrmer, 2015 [73]	0.012	2.032
koln-2017	dense unrimed aggregates	Hogan et al., 2017 [76]	0.158	2.1
leinonen B0 p1	subsequent aggregation of ice crystals and riming—LWP = 1 kg m^{-2}	Leinonen & Szyrmer, 2015 [73]	0.024	1.989
captivate	mass–size relation given by Brown and Francis, 1995 [78] and the area-size relation of Francis et al., 1998 [79]	Mason et al., 2023 [57]	0.012	1.9
leinonen B0 p2	subsequent aggregation of ice crystals and riming—LWP = 2 kg m^{-2}	Leinonen & Szyrmer, 2015 [73]	0.037	1.969
leinonen C	snowflake growth driven primarily by the riming process	Leinonen & Szyrmer, 2015 [73]	469	3.36

Moreover, the particle size distributions (PSD) are assumed to be as gamma distributions, with N0, D_m, and μ calculated in order to match both the D_m and the IWC (derived from the CAPTIVATE retrievals) and the observed CPR reflectivity. Moreover, for each observation, a clear-sky simulated TB vector was estimated by considering only the emission/absorption effect of the gases (oxygen and water vapor) present in the atmosphere (using the ECMWF model temperature and water vapor profiles).

2.4. The AWS-CloudSat Cloud Radiation TB Dataset

The first part of the study consists of a comparison between the simulated TBs at 94 GHz and the CloudSat 94 GHz TBs (2B-TB94 product) for a dataset obtained by selecting CAPTIVATE profiles over ice-free ocean; the analysis was limited to this type of surface because it is characterized by a well-constrained surface emissivity (see Section 2.5). Moreover, the analysis was limited to a temperature below 277 K, which includes 80% of the snowfall events retrieved by the CAPTIVATE algorithm. Besides the CAPTIVATE microphysics profiles, some environmental model derived variables, used as inputs in the TESSEM emissivity model and in the RTM, were included in the dataset. In addition, the corresponding CPR 94 GHz TBs associated with each profile and used as reference (referred to as "observed TBs") were also included. The dataset characteristics and the list of variables included are summarized in Tables 2 and 3. Also, the whole set of AWS-MWR channels has been simulated.

Table 2. Key AWS-CloudSat Cloud Radiation dataset characteristics.

Period	1 January 2007–7 January 2007
Background Surface	Open Water
Temperature Range	<277 K
Number Profiles	1.6×10^5
Number of Snowfall Profiles	6.8×10^4
Number of snowfall profiles with SLW	5.1×10^4

Table 3. Key AWS-CloudSat Cloud Radiation dataset variables.

Variables in the Dataset	Data Source
Ice Water Content (IWC)	CAPTIVATE output
Rain Water Content (RWC)	CAPTIVATE output
Liquid Water Content (LWC)	CAPTIVATE output
Total Precipitable Water (TPW)	ECMWF-AUX
Skin Temperature (T_{sk})	ECMWF-AUX
2 m Temperature (T_{2m})	ECMWF-AUX
Surface Pressure (P_{surf})	ECMWF-AUX
Wind Surface Speed	ECMWF-AUX
Sea Salinity	ECMWF-AUX
Temperature Profile	ECMWF-AUX
Relative Humidity Profile	ECMWF-AUX
Specific Humidity Profile	ECMWF-AUX
Pressure Profile	ECMWF-AUX
CloudSat TB 94 GHz	2B-94TB product

2.5. Microwave Radiometers

In addition to the CPR 2B-TB94 product, we have compared the RTM simulations with PMW measurements from existing radiometers nearly coincident with CloudSat/CALIPSO observations for specific case studies. The purpose is to analyze the measured multi-channel TB signal in presence the of snowfall [27], to verify how they compare with the CloudSat/CALIPSO based RTM model simulations, and to assess the impact of different assumptions on the single scattering model and of SLW layers in the cloud. In particular, TBs observed by the cross-track scanning radiometers Atmospheric Measurement Sounding Unit-A (AMSU-A) and Microwave Humidity Sounder (MHS) are used. The MHS has five channels which cover the frequency range between 89 GHz and 190 GHz, with a 16 km instantaneous field of view (IFOV) at nadir, while AMSU-A is a 15-channel radiometer which covers the frequency range between 23 GHz and 89 GHz, with a 48 km IFOV at nadir. These radiometers, available on board the NOAA-18 and the MetOp-A satellites in the year 2007, were chosen for the comparison because they are cross-track scanning radiometers, like MWR, and they have several channels in common with the MWR onboard AWS, except for the four 325.15 GHz channels. For the comparison between the simulated TBs (based on CPR profiles) and the measured AMSU-A/MHS TBs, the radiometer viewing angle corresponding to each CPR pixel along the CloudSat track intersecting the radiometer swath was taken into account in the RTM simulations (see also Ref. [54]). Moreover, the effect of the different spatial resolution between the CPR and radiometer observations and the time lag between the observations has to be taken into account to correctly compare the observations.

2.6. Arctic Weather Satellite—Microwave Radiometer

The ESA prototype Arctic Weather Satellite (AWS) mission was launched on 16 August 2024. The AWS Microwave Radiometer (MWR) is a 19-channel cross-track scanning radiometer consisting of a rotating antenna focusing the incoming radiation onto four feedhorns (one for each group of channels) and four receivers, covering the frequency range 50–325 GHz (see Table 4). The most innovative aspect of the AWS-MWR with respect

to previous radiometers is the availability of 4 channels in the water vapor absorption band at 325.15 GHz. Each of these channels was designed to be coupled with the corresponding channel in the water vapor absorption band at 183.31 GHz having a weighting function peaking at the same height (see Figure 1). For these two groups of channels in the 325.15 GHz and 183.31 GHz bands, the scattering effects due to the presence of falling snow and cloud ice is expected to be very different, although for "coupled channels" the effect due to water vapor absorption is expected to be very similar.

Table 4. Key AWS-MWR characteristics.

No	Central Frequency (GHz)	Bandwidth (MHz)	NEΔT (K)	Footprint (km)	Polarization	Utilization
1	50.3	180	<0.6	≤40	QV	Temperature Sounding
2	52.8	400	<0.4	≤40	QV	Temperature Sounding
3	53.246	300	<0.4	≤40	QV	Temperature Sounding
4	53.596	370	<0.4	≤40	QV	Temperature Sounding
5	54.4	400	<0.4	≤40	QV	Temperature Sounding
6	54.94	400	<0.4	≤40	QV	Temperature Sounding
7	55.5	330	<0.5	≤40	QV	Temperature Sounding
8	57.290344	330	<0.6	≤40	QV	Temperature Sounding
9	89	4000	<0.3	≤20	QV	Window and Cloud Detection
10	165	2800	<0.6	≤10	QV	Window/Humidity Sounding
11	176.311	2000	<0.7	≤10	QV	Humidity Sounding
12	178.311	2000	<0.7	≤10	QV	Humidity Sounding
13	180.311	1000	<1	≤10	QV	Humidity Sounding
14	181.311	1000	<1	≤10	QV	Humidity Sounding
15	182.311	500	<1.3	≤10	QV	Humidity Sounding
16	325.15 ± 1.2	800	<1.7	≤10	QV	Humidity Sounding/ Cloud Detection
17	325.15 ± 2.4	1200	<1.4	≤10	QV	Humidity Sounding/ Cloud Detection
18	325.15 ± 4.1	1800	<1.2	≤10	QV	Humidity Sounding/ Cloud Detection
19	325.15 ± 6.6	2800	<1	≤10	QV	Humidity Sounding/ Cloud Detection

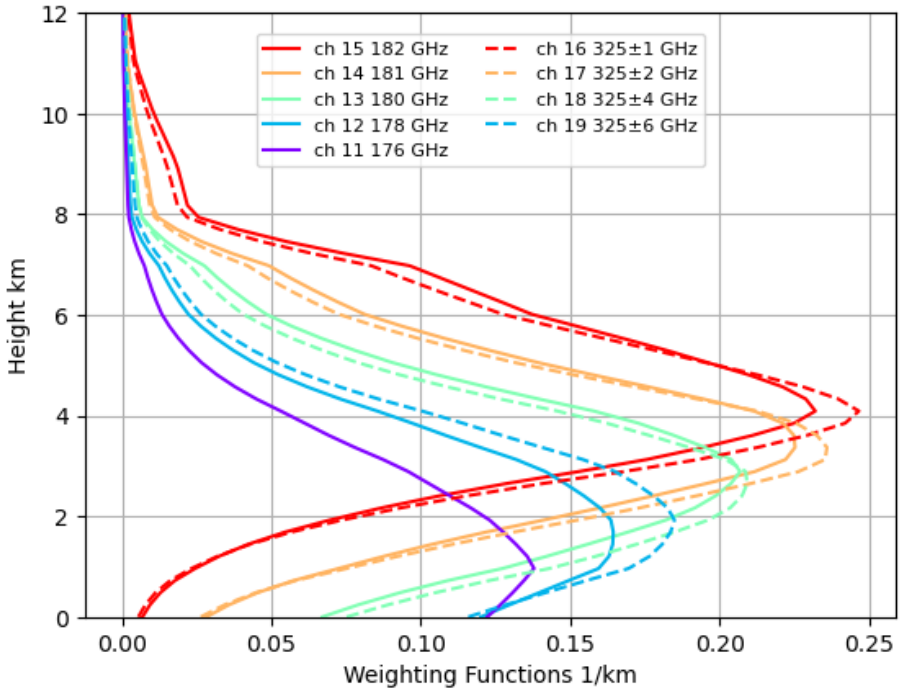


Figure 1. Clear-sky weighting functions for AWS-MWR 183 and 325 GHz channels for the subarctic-winter standard atmosphere [80].

2.7. Methodology

Several case studies of snowfall events were analyzed; one of them, which consists of an intense snowfall event over the Atlantic Ocean, is reported in Section 3.2. The simulated TBs were compared both with the CloudSat TBs and with other nearly-coincident PMW radiometer observations to highlight and interpret the discrepancies between the modeled and measured TBs. In particular, their sensitivity to the scattering models used in the RTM simulations and to the occurrence or lack of SLW layers in the CAPTIVATE profiles was analyzed. Due to the missed detection of SLW layers embedded in the cloud from CPR/CALIOP measurements, some scenarios were obtained by adding SLW layers embedded in the cloud. Different RTM simulations based on different assumptions on the SLW layer (namely, its altitude and its optical depth) were carried out to analyze the simulated multi-channel TB sensitivity to the SLW layer characteristics and to infer the most likely scenarios when compared to the measured TBs. Finally, the multi-channel AWS-MWR TBs were simulated for these scenarios in order to analyze the instrument capabilities to detect the presence of SLW layers embedded in the cloud, and to ultimately retrieve the SLW properties in snowfall conditions.

3. Results

3.1. Analysis of the Cloud Radiation Dataset

First of all, an analysis over clear-sky observations, obtained by applying the radiative transfer model described in Section 2.3, was carried out. A mean constant bias of −4.33 K between the simulated TBs and the 94 GHz CloudSat TB in clear-sky was found in the dataset. Therefore, a bias correction of −4.33 K was applied to the simulated TBs at 94 GHz in the whole dataset. Therefore, a comparison between the 94 GHz simulated TB and the 2B-TB94 product was carried out over the CPR observational dataset (similarly to Battaglia and Panegrossi, 2020 [13]). This type of analysis is very useful because the combined information of perfectly co-located 2B-94TB and CAPTIVATE retrievals from which simulated TBs are derived is fundamental to analyze the cloud ice/snow scattering contribution with respect to the SLW layers emission contribution.

Each panel in Figure 2 shows the differences between the mean 2B-94TB (TB_{obs}) computed for different integrated ice water content (ice water path—IWP) bins and the corresponding mean simulated clear-sky TBs (TB_{cs}) (magenta dashed line) with the corresponding standard deviation (magenta shaded area). The plots were obtained either from the whole dataset (Figure 2a), or only the profiles where CAPTIVATE retrieves SLW (Figure 2b), or only the profiles where CAPTIVATE does not detect SLW (Figure 2c). Each panel also shows the differences between the mean simulated TBs obtained from the same profiles using the 6 different R-G models (TB_{sim}) listed in Table 1 and the corresponding clear-sky TB (TB_{cs}) (continuous lines). From Figure 2a, it is possible to observe that TB_{obs} is always higher than the simulated TB in clear-sky conditions ($\Delta TB_{obs\text{-}CS} > 0$ K), while TB_{sim} becomes lower than the clear-sky conditions ($\Delta TB_{sim\text{-}CS} < 0$ K) for different IWP thresholds which depends on the R-G model used in the simulations. It is evident that as the IWP increases, the cooling effect on TB_{sim} due to the scattering by the cloud ice and snowfall increases, but the behavior strongly depends on the R-G model used. Leinonen A0 is the model where the scattering effect is the weakest, and seems to match more closely the observations, while leinonen C is the model where the scattering effect is the strongest, deviating very significantly from the observations.

In Figure 2b,c, the differences between simulated and observed TBs become even larger for observations where CAPTIVATE does not detect SLW, while a better agreement is achieved where CAPTIVATE detects SLW (and therefore the retrieved LWC is included in the RTM simulations), except for high IWP values. The combination of these results can be possibly explained by the missed detection by CPR/CALIOP of SLW layers in the cloud described in Sections 1 and 2. The RTM simulations of the TB_{sim}, derived from the CAPTIVATE profiles, cannot capture the emission effect of the not-detected SLW layers. Therefore, in our simulations which are based on the CAPTIVATE retrievals, the scattering

effect dominates, especially in profiles where CAPTIVATE does not retrieve the presence of SLW, leading to TB cooling (on average) with respect to the clear-sky signal. This behavior does not find correspondence in the observed TBs (2B-94TB). Figure 2 evidences that the problem is independent of the R-G model used in the simulations.

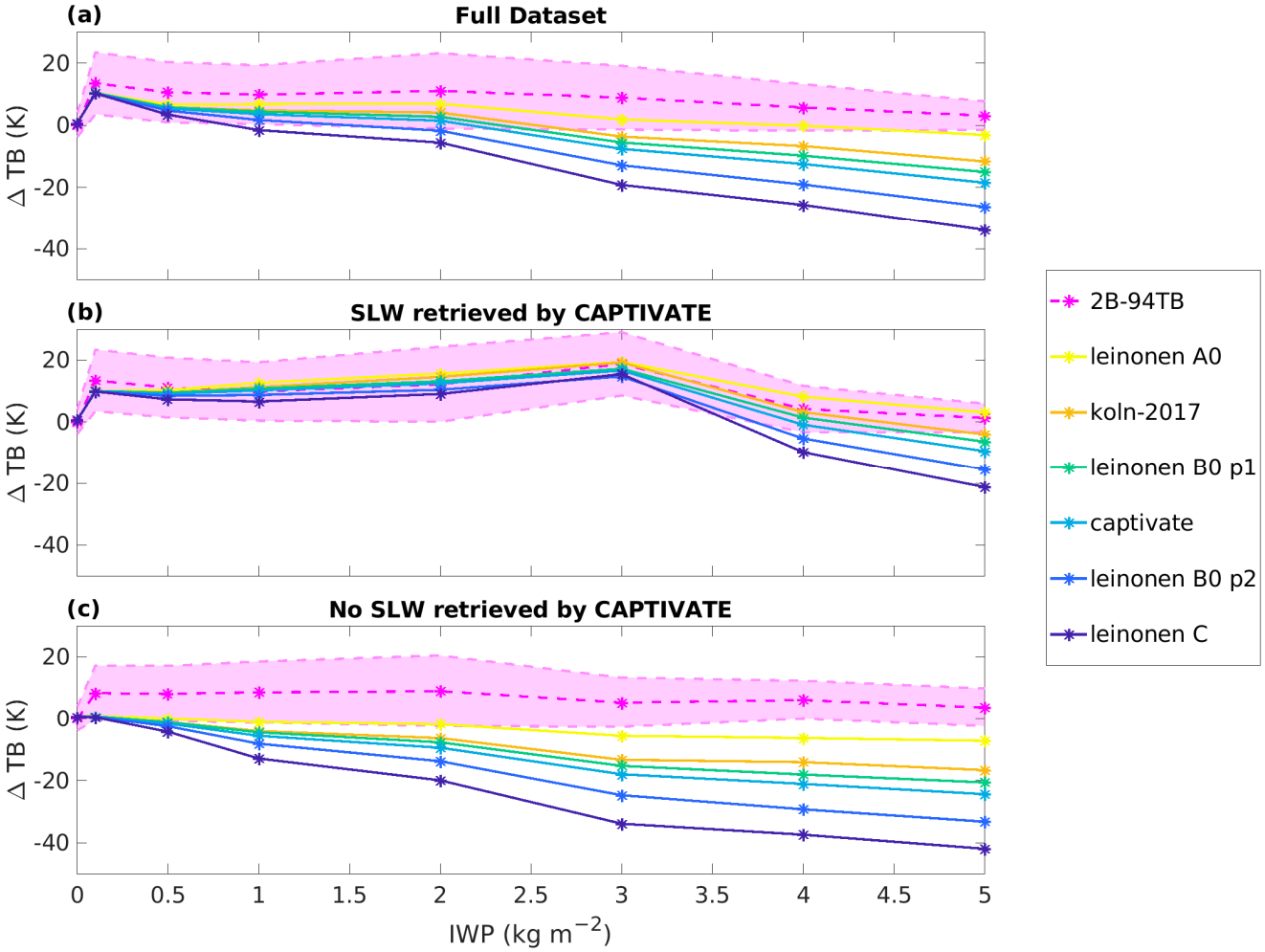


Figure 2. Differences between 2B-94TB TBs and clear-sky simulated TBs (dashed magenta line) and between simulated TBs obtained by using several R-G models and clear-sky simulated TBs (continuous lines) for the whole dataset (**a**), for observations where CAPTIVATE detects SLW (**b**), and for observations where CAPTIVATE does not detect SLW (**c**). The shaded magenta area represents the standard deviation of the differences between 2B-94TB (dashed magenta line) and the clear-sky simulated TBs within each IWP bin. The plotted point for IWC = 0 kg m^{-2} represents clear-sky conditions.

The hypothesis that the differences between simulated TBs and the 2B-94TB product are due to missed detection of SLW layers is also supported by the results in Figure 3, where the observations where CAPTIVATE does not detect SLW (the same as in Figure 2c) are reported in an IWP-$\Delta TB_{sim\text{-}obs}$ plane. In Figure 3a, the number of snowfall observation occurrences is reported, while in Figure 3b, the mean differences between the observed TBs and the simulated TBs in clear-sky conditions ($\Delta TB_{obs\text{-}cs}$) calculated for each bin are reported. This difference indicates the presence of a dominant emission effect from the cloud system when its values are positive ($TB_{obs} > TB_{CS}$), and a dominant scattering effect when its values are negative ($TB_{obs} < TB_{CS}$). TB_{sim} are computed using the leinonen A0 R-G scattering model, which shows the least pronounced scattering effect compared to the other models reported in Figure 2. It is worth noting that the mean $\Delta TB_{sim\text{-}obs}$ values (black

line) are always negative. This is due to the fact that, when the CAPTIVATE algorithm does not detect SLW, TB_{sim} is generally lower than TB_{obs}, even if the R-G model with the lighter scattering effect is considered. Moreover, the lower (negative) $\Delta TB_{sim\text{-}obs}$ values match with the bins where the most evident emission effect is found in the observations ($\Delta TB_{obs\text{-}cs} > 0$ K, red bins); the few bins where the observations show TB cooling with respect to the clear sky, indicating the predominance of the scattering effect ($\Delta TB_{obs\text{-}cs} < 0$ K, blue bins), match with positive (or nearly 0 K) $\Delta TB_{sim\text{-}obs}$ values. This observed correlation between the most pronounced emission effect and the bins where the $\Delta TB_{sim\text{-}obs}$ are negative, and the absence of an emission effect—or even the presence of a light scattering effect—in bins where $\Delta TB_{sim\text{-}obs}$ are nearly 0 K or positive, is consistent with the hypothesis that the discrepancies between observations and simulations are due to the missed detection of SLW by the CAPTIVATE algorithm.

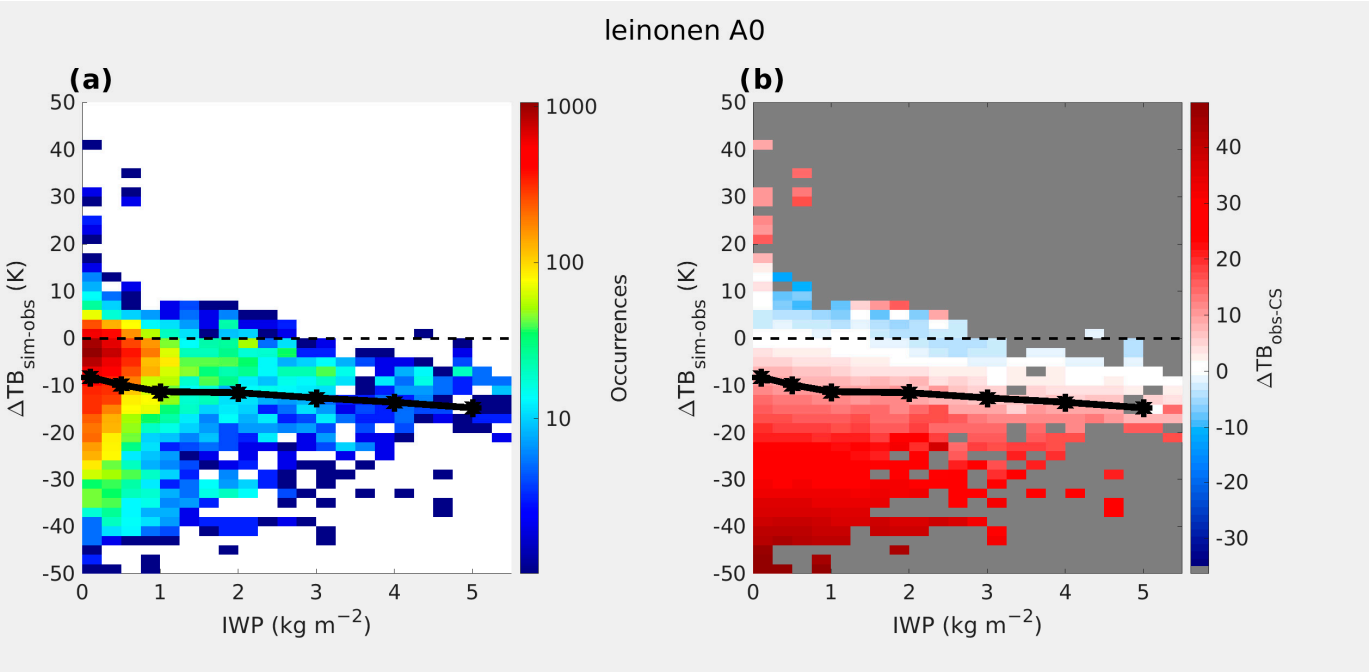


Figure 3. 2D histogram of the occurrences (**a**) and of the mean $\Delta TB_{obs\text{-}CS}$ (**b**) in an IWP/$\Delta TB_{sim\text{-}obs}$ plane (R-G model: Leinonen A0) for observations where SLW is not detected by the CAPTIVATE algorithm. Bins are characterized by 0.25 kg m^{-2} and 4 K intervals. The continuous black line represents the mean value for the same IWP bins of Figure 2.

The current hypothesis is also supported by the analysis of observations where SLW is detected by the CAPTIVATE algorithm. Figure 4 shows the mean difference between the simulated TBs at 94 GHz and the 2B-94TB product TBs ($\Delta TB_{sim\text{-}obs}$) as a function of IWP and for different values of SLW path (SLWP, as derived from the CAPTIVATE profiles in the AWS-CloudSat cloud radiation dataset). The SLWP is the vertically integrated LWC retrieved by CAPTIVATE above the freezing level height. It is possible to observe that the differences are negative for snowfall observations without SLW layers (cyan curve, the same shown in Figure 3), are close to 0 for values between 0.1 kg m^{-2} and 0.2 kg m^{-2} and are positive for values higher than 0.3 kg m^{-2}. It is possible to assume that the negative differences ($TB_{sim} < TB_{obs}$) are due to the missed detection of SLW layers if embedded in the clouds, while the positive differences ($TB_{sim} > TB_{obs}$) are due to a SLWP overestimation by the CAPTIVATE algorithm which mostly retrieves SLW layer near the cloud top.

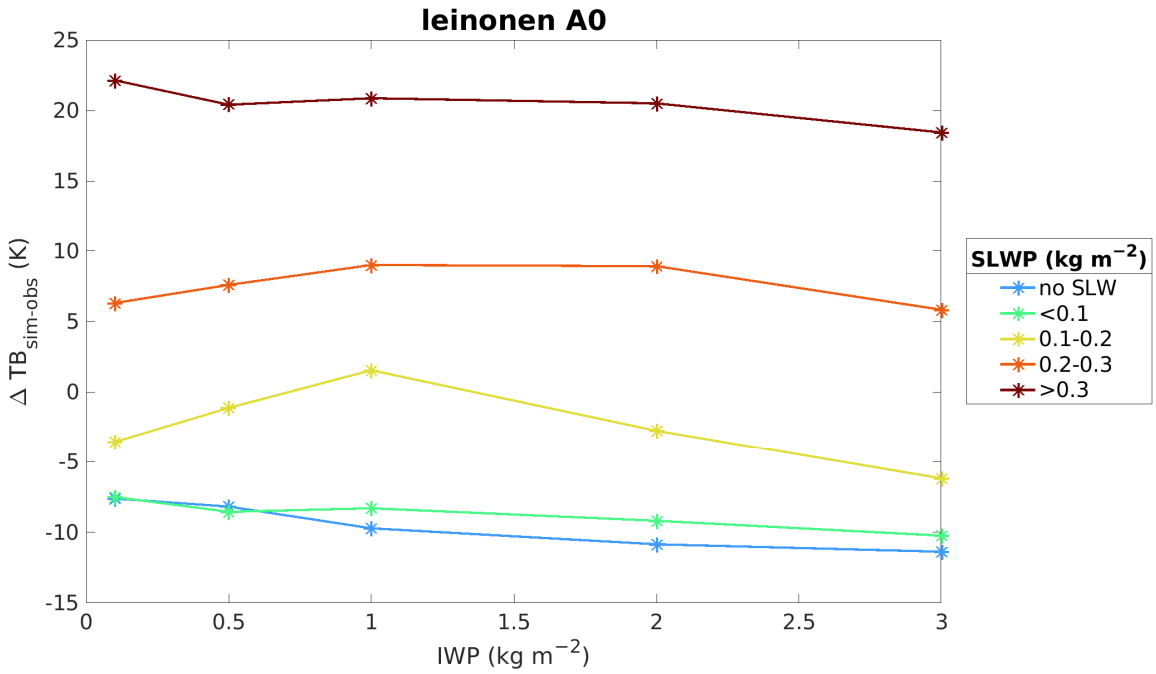


Figure 4. Comparison of $\Delta TB_{sim\text{-}obs}$ (R-G model: Leinonen A0) as a function of IWP (same bins of Figure 2) for different bins of SLWP.

3.2. Analysis of the Case Study

The analysis shown in Section 3.1 of the snowfall dataset is limited to the comparison between simulations and observations at 94 GHz. Here, a case study for which nearly coincident measurements by CloudSat/CALIPSO and by multi-channel cross-track scanning passive MW radiometers are available is analyzed in detail. The goal is to show how the simulated TBs (TB_{sim}) derived from the CAPTIVATE SLW and ice/snow profiles compare with the measured TBs (TB_{obs}) at different frequencies close to some of the AWS-MWR channels, and to investigate how different scenarios of distributions and amounts of SLW, embedded in the cloud, might affect the simulated TBs.

The case study refers to an intense snowfall event that occurred over the North Atlantic near the island of Newfoundland on 1 January 2007. CPR overpassed the event between 05:32:07 UTC and 05:37:27 UTC; the temporally closest radiometer observations are those obtained by the AMSU-A and MHS onboard NOAA-18 (between 5:11:03 UTC and 05:16:34 UTC, with a time difference of 21 min). MHS observed the event within a viewing angle between 22° and 20°, AMSU-A observed the event with a viewing angle between 28° and 20°, and TBs are simulated considering the corresponding viewing angle. It is worth noting that each CPR profile is associated with the nearest radiometer footprint by applying a k-nearest neighbor algorithm which considers the coordinates of the CPR tracks and those of the center of the MW radiometer pixels; therefore, the obtained TB_{sim} obtained from the CPR profiles associated to the same AMSU-A or MHS pixel have been averaged to match the PMW footprint.

Figure 5 shows the TB imagery of the MHS channel at 190.31 GHz (a) and the AMSU-A channel at 50.3 GHz (b). The CloudSat track is shown in red on both images. An extensive cyclonic system over ice-free ocean, characterized by a widespread frontal snowfall event, is clearly visible in both images, as an area of TB cooling at 190.31 GHz, due to the dominant effect of the scattering by cloud ice and snow at this frequency, and an area of TB warming at 50.3 GHz, likely due to the emission by liquid water. The CPR captures the western side of the deep frontal system.

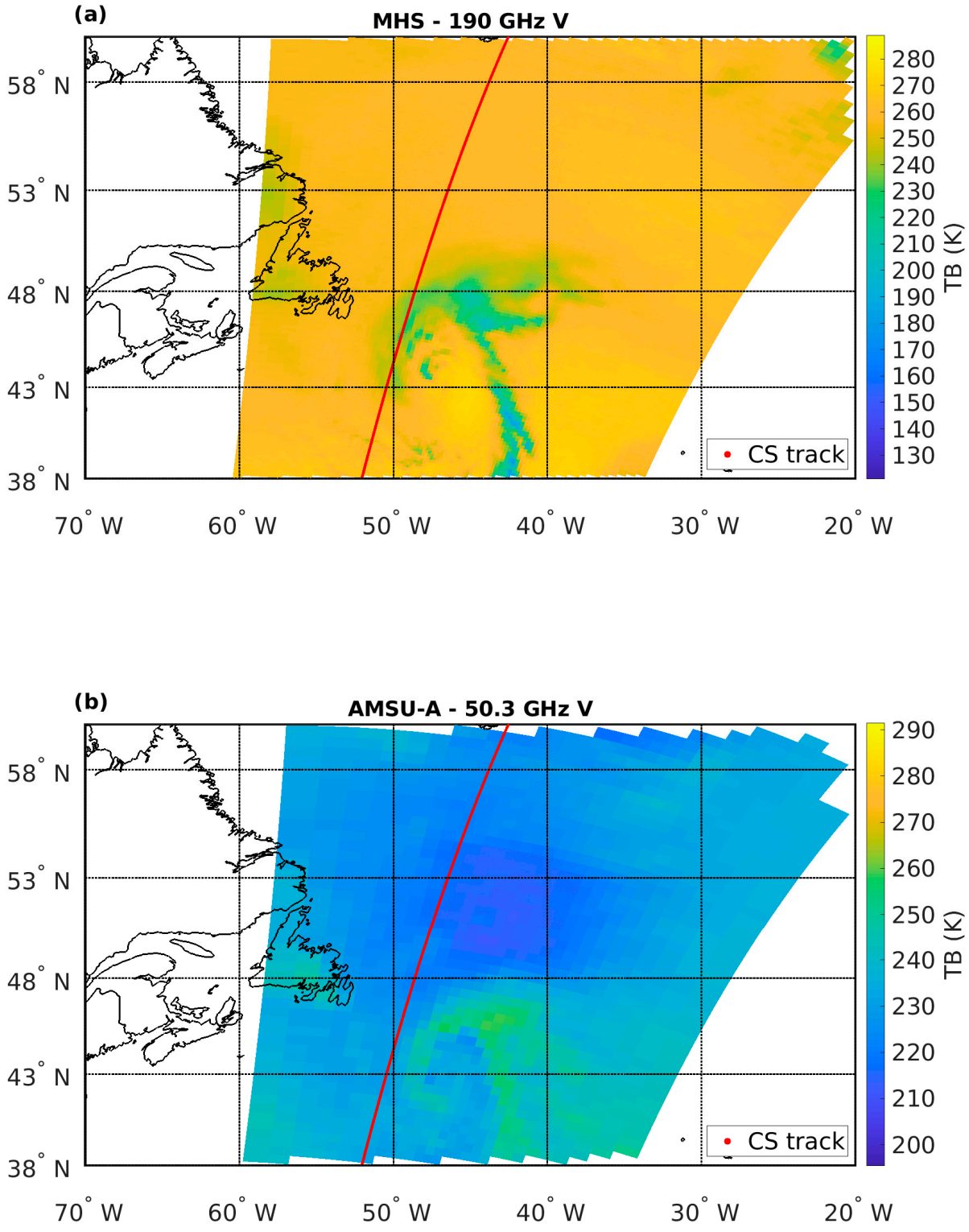


Figure 5. Case study off Newfoundland: MHS 190.31 GHz TBs (**a**) and AMSU-A 50.3 GHz TBs (**b**) onboard NOAA-18 (orbit number: 8329, descending mode). CloudSat track (CloudSat orbit number: 3609) is reported in red.

In Figure 6, the imagery of CPR reflectivity (a), CAPTIVATE IWC (b), and LWC (c) are shown, and the corresponding IWP and liquid water path (LWP) along the CloudSat track (d) and the TPW and T_{2m} obtained from ECMWF-AUX product (e) are also reported. The event shows an intense snowfall region with distinct deep convection features, and a large anvil extending to the north. The deepest cloud between 43°N and 48°N shows the

highest radar reflectivity around 10–15 dBz, cloud top height around 8 km, and IWP values reaching 6 kg m^{-2}. The peak IWP values are associated with particularly high IWC located above 5–6 km. Shallow snowfall structures also appear as a distinctive separate cloud structure north of about 52°N, although embedded shallow convective structures are also evident in the lowest ~1 km (e.g., at 54°N). In the southern part, it is very likely that there was a transition to mixed-phase or liquid precipitation (T_{2m} > 277 K and TPW > 10 mm). It is worth noting that the CAPTIVATE algorithm identified the presence of SLW (magenta layers in the top panel) only in presence of the shallower cloud systems in the northern part and in the southern part of the event (lat < 42°N), while it does not identify the presence of SLW layers in the deep and intense snowfall event (42°N < lat < 52°N). The LWP is highly variable along the track, with values mostly below 1 kg m^{-2}.

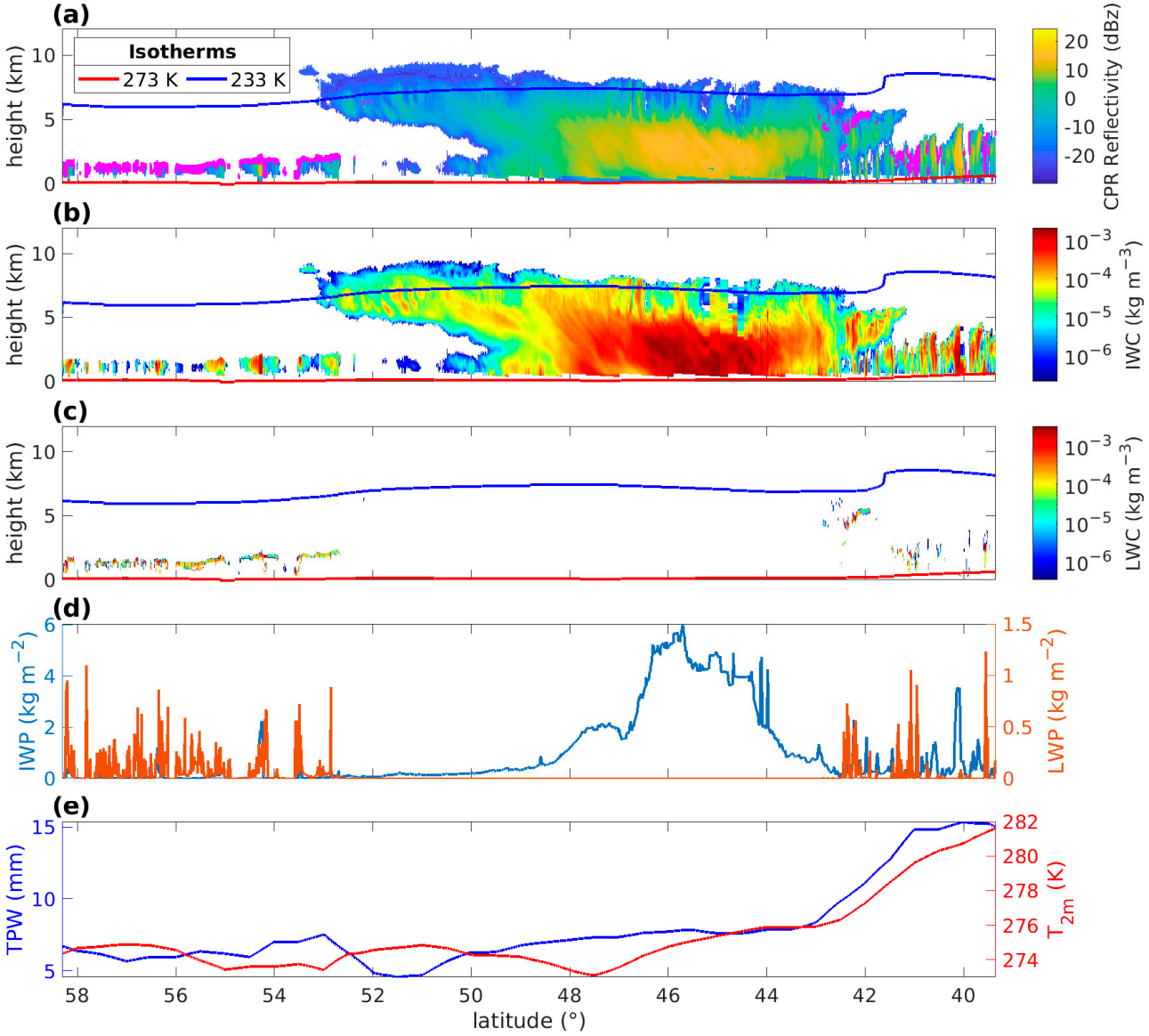


Figure 6. Case study off Newfoundland: Height–latitude imagery of CloudSat CPR reflectivity (**a**), CAPTIVATE Ice Water Content (**b**), Liquid Water Content (**c**). Retrieved IWP (blue curve) and LWP (red curve) are shown in (**d**). (**e**) ECMWF TPW and T_{2m} values. In (**a**), magenta dots represent CPR bins where SLW is detected by CAPTIVATE algorithm. In (**a**–**c**), freezing level (273 K isotherm, red line) and −40 °C isotherm (233 K isotherm, blue line) are also shown.

3.2.1. Comparison of Multi-Channel Simulated and Measured Brightness Temperatures

The comparison between the CPR 2B-94TB product and MHS measured TBs (TB_{obs}) with the simulated TBs (TB_{sim}) obtained by applying several R-G models is illustrated in Figures 7 and 8. In Figure 7, the TB_{sim} is shown for six different R-G models, along with the corresponding clear-sky simulated TB (TB_{cs}—green dotted line) and the 2B-94TB product TB_{obs} (magenta dashed line). It is worth noting that all simulated TBs show a clear TB cooling with respect to the clear-sky values in the most intense part of the snowfall event (42°N < lat < 48°N, see Figure 6), although with different intensity depending on the R-G model used (from −5 K for leinonen A0 model to −40 K for leinonen C0 model). This behavior is in contrast with the observations (TB_{obs}) which are quite similar to the simulated clear-sky TBs in this region (likely because the emission effect by embedded SLW water balances the scattering effect due to cloud ice/snow). On the other hand, an increase of the TB_{obs} with respect to the clear-sky conditions (up to +20 K) is present in the cloud anvil (48°N < lat < 52°N, see Figure 6d). This behavior is not reproduced by any of the RTM model simulations. A good agreement can be observed between TB_{sim} (regardless of the R-G model used) and TB_{obs}, for the shallow cloud system north of 52°N (see Figure 6a), where CAPTIVATE detects a layer of SLW on top of very shallow clouds. In this region both TB_{sim} and TB_{obs} increase with respect to the clear-sky conditions, although the increase is generally higher for the TB_{sim}. South of 43°N, in moister and warmer environmental conditions (see Figure 6), the TB_{sim} oscillates with an intensity modulated by the partitioning between the IWP and the LWP (e.g., TB_{sim} warming is observed only in correspondence of the peaks of the LWP, while a TB_{sim} cooling is observed in correspondence of a peak of IWP and of a low value of LWP).

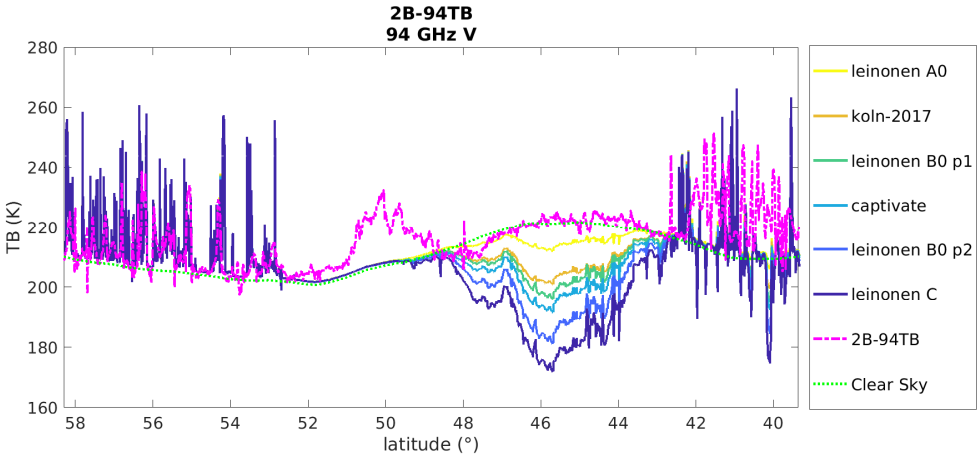


Figure 7. Case study off Newfoundland: Comparison between TB_{sim} at 94 GHz obtained by using six different R-G models (as indicated in the legend), 2B-94TB product (TB_{obs}, magenta line), and clear-sky simulated TBs (TB_{CS}, green dotted line). See Figure 6 for CPR reflectivity, SLW position, and IWP/LWP values.

Figure 8 shows the comparison between the MHS measured TBs at 89 GHz V (a), 157 GHz V (b), and the 190 GHz V (c) and the corresponding simulated TBs obtained by applying the same six different R-G scattering models used for Figure 7. The comparison at 89 GHz shows a similar pattern to that identified at 94 GHz in Figure 7. Also, the MHS 89 GHz shows a TB warming (up to 15 K with respect to the clear-sky conditions) in correspondence of the cloud anvil and almost no cooling in correspondence of the deeper part of the cloud, while a TB cooling can be observed for the simulated signal (from −10 K to −50 K depending on the scattering model used). The differences derive from the different resolutions, the different time of overpass and the difference of frequency, although small; e.g., the TB warming in the shallow clouds system in the northern sector (north of 52°N) is less evident than in Figure 7 because of the finer spatial resolution of the CPR product

with respect to the MHS radiometer. For the 157 GHz channel, both simulations and observations show a significant TB cooling (with respect to the clear-sky conditions) in the most intense part of the snowfall event (42°N < lat < 48°N); however, the TB cooling is much larger for TB_{sim} (dropping by −70 K for the leinonen B0 p2 model) than for the TB_{obs} (max TB depression −25 K), with the only exception of the leinonen A0 and koln-2017 models. Even at this frequency it is possible to observe an increase of the MHS TBs in the cloud anvil (48°N < lat < 52°N, up to +10 K with respect to the clear-sky conditions), which is not reproduced by any of the R-G simulations. For the 190 GHz channel, both the TB_{sim} and the MHS TB_{obs} show a significant cooling in the most intense part of the snowfall event (42°N < lat < 48°N). The TB_{sim} cooling effect varies among the different models: the leinonen A0 and koln-2017 models underestimate the cooling effect observed in the MHS TBs (max TB depression −15 K and −10 K, respectively) while leinonen B0 p2 tends to overestimate this effect (max TB depression −35 K). Leinonen B0 p1, leinonen C, and the captivate models are in good agreement with the observed MHS TBs. For this channel, the increase of the MHS TBs in the cloud anvil (48°N < lat < 52°N) is not observed. The absence of an emission signal is also visible in the MHS 190.31 GHz TB imagery (Figure 5a), along the CloudSat track.

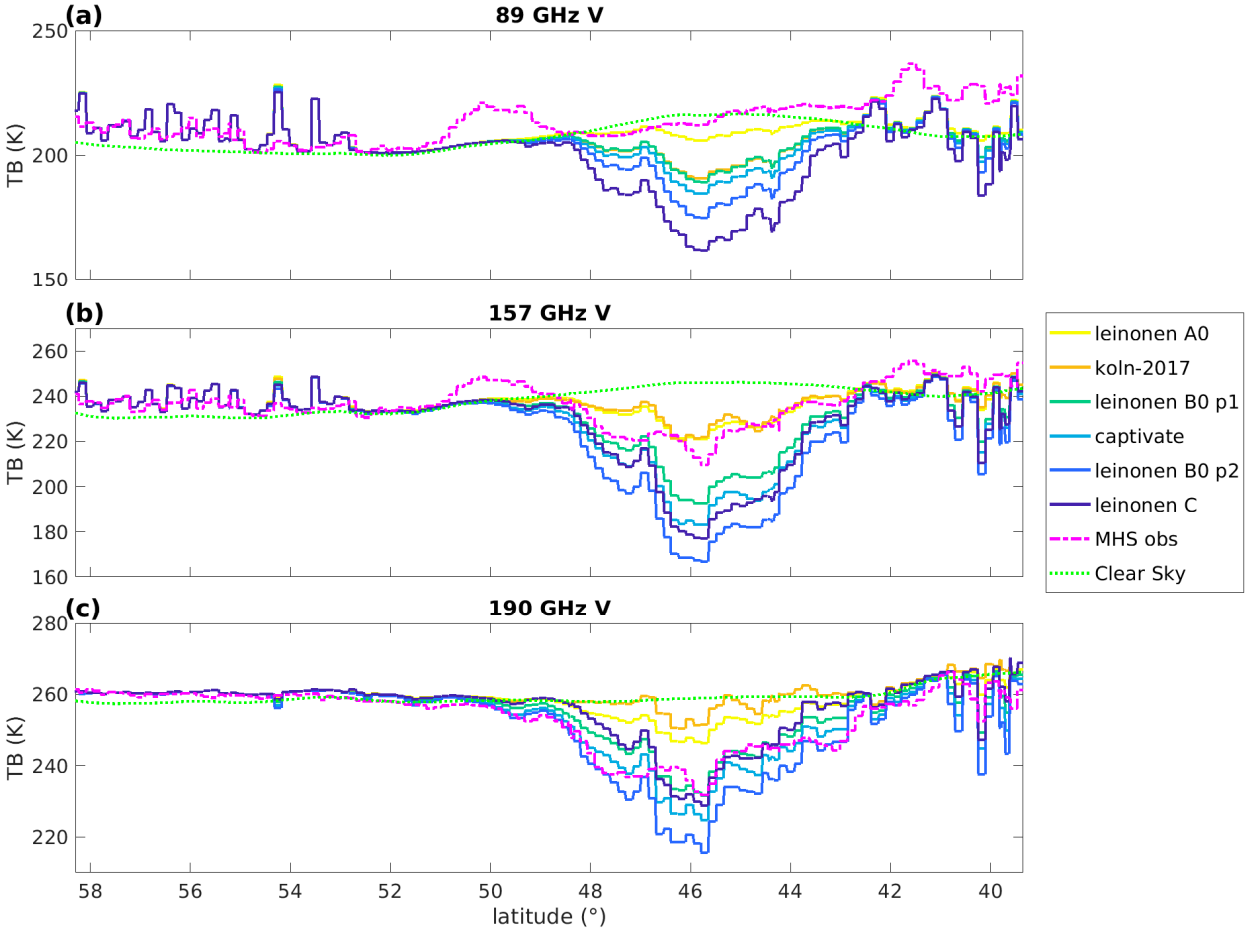


Figure 8. Case study off Newfoundland: Comparison between the TB_{sim} obtained by using six different R-G models (indicated in the legend) and MHS TB_{obs} at 89 GHz (**a**), 157 GHz (**b**), and 190 GHz (**c**). The magenta dashed line represents the MHS measured TBs (TB_{obs}), while the green dotted line represents the clear-sky TBs (TB_{CS}). See Figure 6 for CPR reflectivity, SLW position, and IWP/LWP values.

The different behavior between the TB_{sim} and the TB_{obs} in the cloud anvil and in the deepest part of the cloud, which is particularly evident for the 89 and 94 GHz channels,

can be attributed to the presence of a SLW layer embedded in the cloud which has not been retrieved by the CAPTIVATE algorithm. The emission from the cloud liquid droplets present in the SLW layers would tend to increase the TBs corresponding to the cloud anvil and would tend to mask (or attenuate) the TB cooling due to the scattering by cloud ice (snowflakes) in the deeper part of the cloud. To prove this, new simulations were performed by adding a 1 km SLW layer to the CAPTIVATE retrievals. The analysis has been conducted first by varying the LWP (three different values are considered, 0.125, 0.18, and 0.25 kg m $^{-2}$) at a fixed location around 4 km above sea level (which roughly corresponds to the 253 K isotherm), and then varying the layer height (between 2 and 6 km above sea level, i.e., between 243 K and 263 K isotherm) fixing the LWP at 0.18 kg m^{-2}. Also, the sensitivity to layer thickness was evaluated by varying this parameter while fixing the layer height and LWP. However, no significant sensitivity to this parameter was observed. It is worth noting that these are idealized scenarios, aimed at evaluating the sensitivity of the simulated TBs to the presence of SLW layers and not at obtaining a perfect coincidence between the simulated and the observed TBs. Certainly, a more realistic scenario would be more likely represented by a combination of SLW layers at different heights with different LWC. The leinonen B p2 R-G scattering model has been used in the simulations in order to obtain a satisfactory agreement with observations at high-frequency channels (especially for MHS 190.31 GHz channels). The models which show lighter scattering effects, such as leinonen A0 and koln-2017, underestimate the cooling effect in the deeper portion of the cloud at 190.31 GHz, even without the addition of a SLW layer.

A strong influence of the variation of the LWP values on the TB increase with respect to the simulation with no SLW is observed (Figure 9a). In particular, a strong TB increase can be observed in the cloud anvil (from +10 to +20 K with respect to the TB_{sim} with no SLW) and a good agreement between the simulated TBs and the 2B-94TB product mean values is obtained in the cloud anvil with a SLW layer that produces a LWP = 0.18 kg m $^{-2}$. Concerning the deeper part of the cloud, the three simulations with different LWP values show higher TBs (by 20–35 K) than the TB_{sim} without SLW, and they get closer to the 2B-94TB product values as the LWP increases. The panels in the right column show a significant increase of the TBs by adding the SLW layer, which approaches the 2B-94TB in both the anvil region and in the deep cloud region as the layer height decreases; a scattering signal (TB cooling with respect to the clear sky) is observed for all three scenarios in the deeper part of the cloud, although it is strongly attenuated with respect to the scenario with no SLW (blue curve).

The same two experiments were carried out by considering the same MHS channels (89 GHz V, 157 GHz V, and 190 GHz V) shown in Figure 8. Figure 10 shows the comparison between the MHS TB_{obs} and the relative TB_{sim} obtained by varying the LWP (a, c, and e, where the layer height is at 4 km above sea level) and the SLW layer height (b, d, and f, where the layer LWP is equal to 0.18 kg m^{-2}).

From Figure 10a,b, where the 89 GHz V channel TBs is shown, it is possible to observe a marked emission signal generated by the presence of the SLW layer resulting in a significant increase of the simulated TBs (10–18 K in the cloud anvil, 20–35 K in the deeper part of the cloud) with respect to the TB_{sim} obtained without the added SLW layer. The variation of the LWP values has a strong impact on the simulated TBs (Figure 10a). A good agreement between the simulated and the MHS TBs mean values is obtained in the cloud anvil for LWP = 0.18 kg m $^{-2}$. Concerning the layer height (Figure 10b), a different impact is evident between the 2 km layer height simulation and the other two layer height simulations, which exhibit a more similar behavior. This behavior shows some similarities with the results at 94 GHz shown in Figure 8; the differences are due to the different spatial resolution and the different viewing angles of MHS and CPR. Concerning the deeper part of the cloud, the five simulations with different LWP values/layer heights show higher TBs than the simulations without SLW. However, they show a scattering signal that is not present in the MHS TBs.

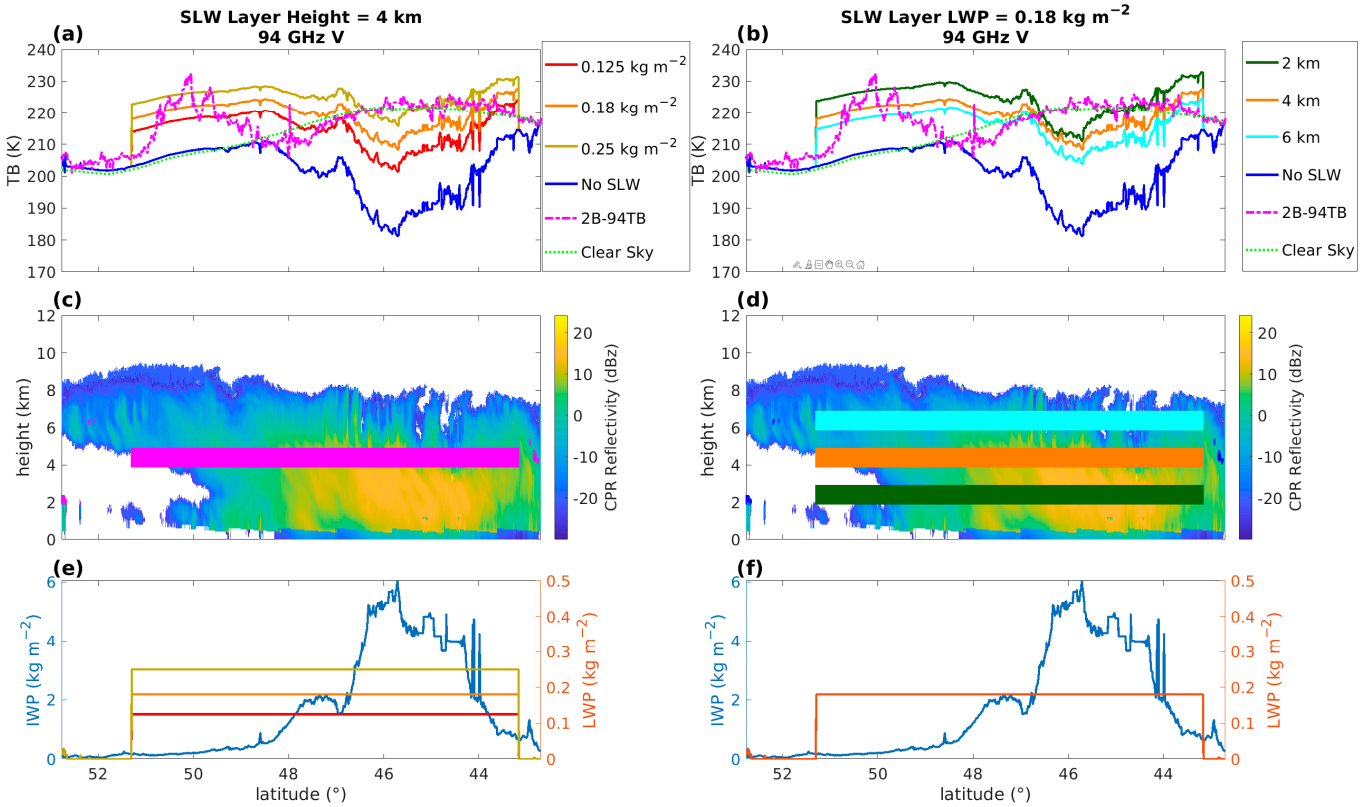


Figure 9. Case Study off Newfoundland: Comparison between the TB_{sim} (R-G model: Leinonen B p2) obtained by adding a SLW layer to the CAPTIVATE scene in correspondence to the 253 K isotherm (**a**) and a SLW layer for a total LWP = 0.18 kg m^{-2} (**b**) and 2B-94TB product TB_{obs}. Three different LWP values (0.125, 0.18, and 0.25 kg m^{-2}) (**a**) and SLW layer heights (2 km, 4 km—which roughly corresponds to the 253 K isotherm—and 6 km—which roughly corresponds to the 243 K isotherm) (**b**) are considered. The magenta dashed line corresponds to the CPR 2B-94TB product, while the green dotted line corresponds to the clear-sky TBs (TB_{CS}) In (**c**,**d**), the CloudSat CPR reflectivity imagery is shown—the magenta stripe (**c**) and the colored stripe (**d**) represent the 1 km SLW layers representing the different scenarios. In (**e**,**f**) the CAPTIVATE-retrieved IWP along the CPR track and the assumed values for the LWP are also shown.

Concerning the 157 GHz channel, the sensitivity of the TB_{sim} to the SLW layer is still significant (5–10 K for the anvil, from 25–45 K for the deeper part of the cloud with respect to the TB_{sim} without the added SLW layer). However, the impact appears to be lower than at 89 GHz because of the larger TB depression due to the scattering by the cloud ice at this frequency. As a result, an evident scattering effect (TB cooling) is visible in the deeper part of the cloud while the TB warming is weaker, although still visible, in the cloud anvil. The influence of different LWP values (Figure 10c) on the TB increase is lower than at 89 GHz, while the differences between the TB_{sim} obtained for different layer heights (Figure 10d) are larger than at 89 GHz. As the frequency increases, the water vapor emission increases the clear-sky TBs (from 200–220 K at 89 GHz to 260 K at 190 GHz), and affects the weighting functions. The impact of the SLW layer on increasing the TBs is visible only if the SLW layer is above the peak of the weighting function.

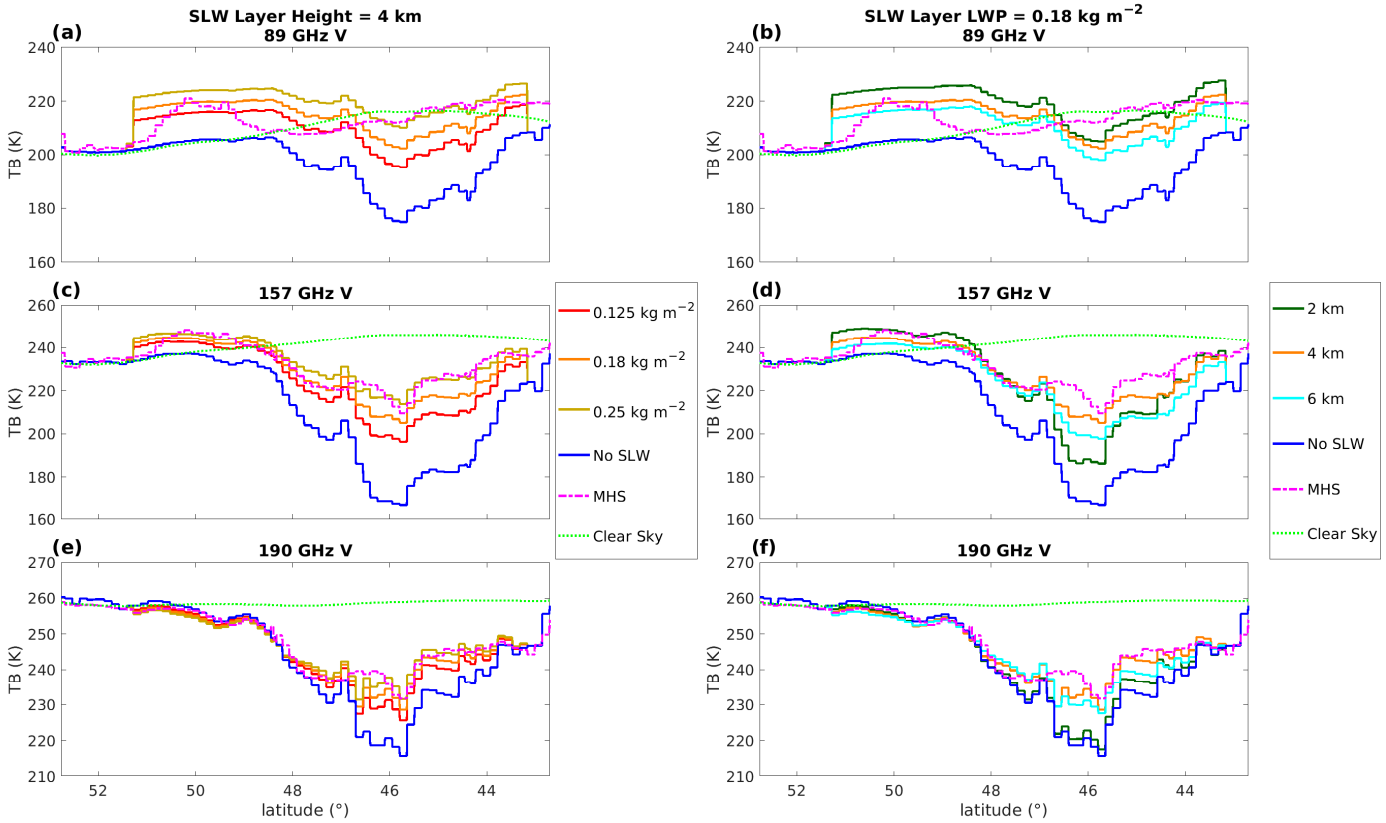


Figure 10. Case Study off Newfoundland: Same as Figure 9, for the MHS 89 GHz (**a**,**b**), 157 (**c**,**d**) GHz, and 190 GHz (**e**,**f**) channels. See Figure 9 and its caption for CPR reflectivity, SLW layers height, and IWP/LWP values, and for the description of the two experiments.

Concerning the 190 GHz V channels the sensitivity to the SLW layer is even lower, and the effect with respect to the simulation without the SLW layer (blue line) is evident only in the deeper part of the cloud as an attenuation of the snow/cloud ice scattering signal. The differences between the TB_{sim} for different LWP values (Figure 10e) are not very significant; the SLW layer at 2 km height (Figure 10f) shows almost no influence (the curve almost overlaps with the blue curve with no SLW), while for the two scenarios with the SLW layers at higher elevation, the emission effect is clearly visible (a $\approx$ +10 K TB warming is visible with respect the TB_{sim} without added SLW) and tends to mask the scattering signal in the region of the deeper cloud. This results in TBs that closely match the MHS measurements. It is worth noting that channel frequencies close to those shown in Figure 10 will be available on AWS-MWR (i.e., 89, 165.5, and 176.31 GHz), and a very similar behavior and sensitivity to the SLW is observed for the AWS-MWR for these channels.

A comparison with the AMSU-A observations, which shares several channels in the 50–60 GHz oxygen absorption band with the AWS-MWR, was also carried out. In Figure 11, a comparison between the AMSU-A TB_{obs} and the relative TB_{sim} obtained by varying the LWP (a, c, and e, where the layer height is 4 km above sea level) and the SLW layer height (b, d, and f, where the layer LWP is equal to 0.18 kg m^{-2}) for three channels in the oxygen absorption band is reported. The top panels, where the 50.3 GHz V channel TBs are shown, show a strong emission signal generated by the presence of the SLW layer. The TB increase (from +4 to +8 K) is highly correlated with the LWP variation (Figure 11a). Concerning the influence of the layer elevation (Figure 11b), the bottom layer is associated with the larger TB increase, while the two higher layers have similar impact on the TBs. At 52.8 GHz there is much lower sensitivity to the presence of SLW; there is almost no sensitivity to the different LWP values (Figure 11c), while there is a slightly larger impact of the layer position on the simulated TBs (Figure 11d). At 53.6 GHz (Figure 11e,f) there is almost

no sensitivity to the presence of SLW. This change in sensitivity to the SLW is due to the increase in height of the weighting function peak as we move towards the center of the 50–60 GHz absorption band (probably at 53.6 GHz the weighting function peaks above the SLW layers). Similar channels with the same central frequencies are also available on AWS-MWR, thus the same sensitivity to SLW is expected for these channels.

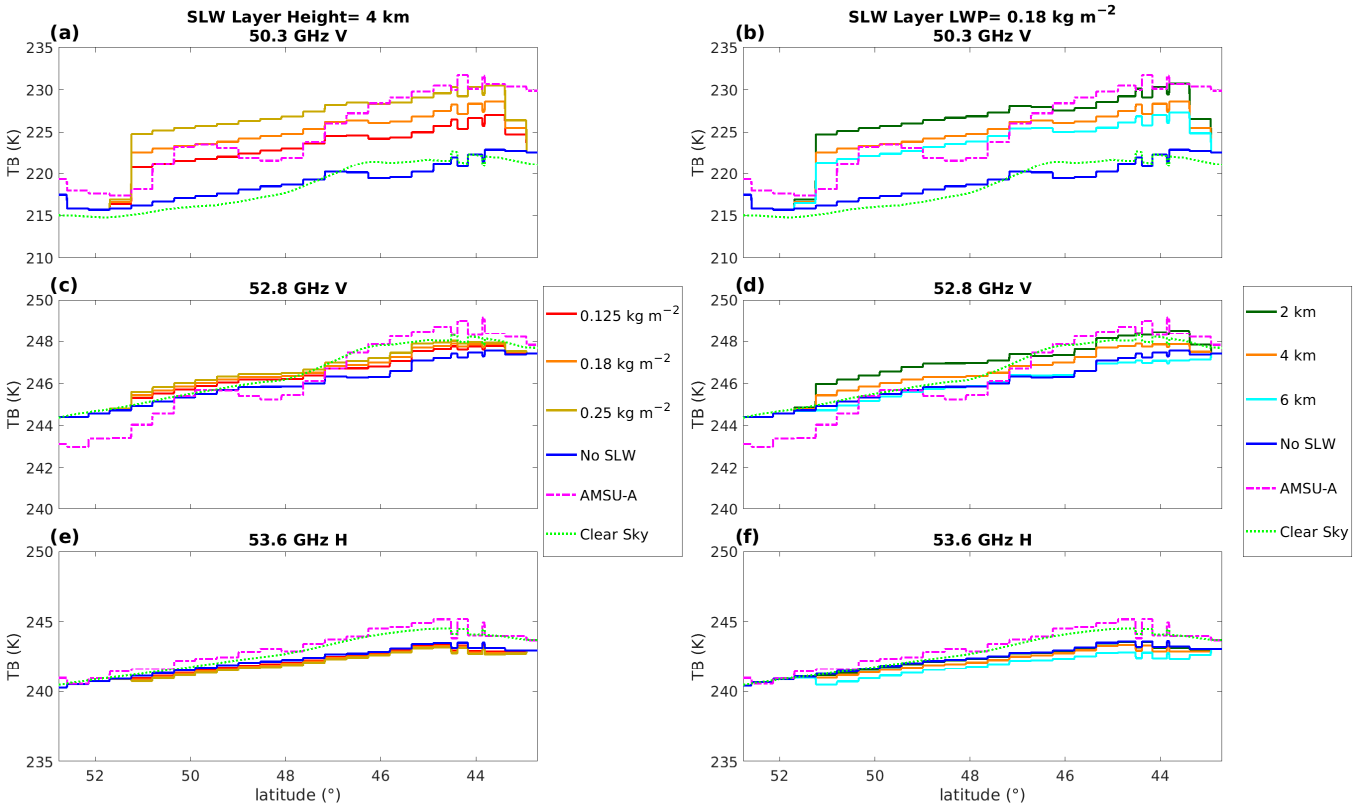


Figure 11. Case Study off Newfoundland: Same as Figure 10, for the AMSU-A 50.3 GHz (**a**,**b**), 52.8 GHz (**c**,**d**), and 53.6 GHz (**e**,**f**) channels. See Figure 9 and its caption for CPR reflectivity, SLW layers height, and IWP/LWP values, and for the description of the two experiments.

This sensitivity analysis shows that there is a strong influence of the SLW layer on the TB signal for the analyzed case study, both in presence of shallow, weak snowfall, and for deep intense snowfall, especially for the channels between 89 and 165 GHz (at 190 GHz only when the SLW layer is at higher levels); the emission effect generated by a small amount of supercooled water (<0.2 kg m^{-2}) can also totally mask the scattering effect generated by the snowflakes. The liquid water amount shows a strong effect on the frequency channels below 90 GHz, while the high-frequency channels are more influenced by the SLW layer position. It is worth noting that the effect of the SLW layers on the measured TB for this case study is influenced by the environmental conditions (mostly the low moisture conditions, with TPW mostly below 6 mm). In such conditions, the effect of the SLW layers can be visible also at higher frequencies, as far as the weighting function of a given channel peaks below the SLW layer.

3.2.2. Added Value of the AWS-MWR 325.15 GHz Channels

One of the innovative aspects of the AWS mission is the availability of the sub-mm channels in the 325.15 GHz water vapor absorption band. These channels are expected to have strong sensitivity to the cloud ice. However, the effect of SLW on these channels needs to be investigated to determine to what extent they, together with their coupled channels in the 183.31 GHz absorption band (see Section 2.3), can contribute to improved snow retrieval in the presence of SLW.

The same configurations described above were used to simulate the AWS-MWR channels. The TBs have been simulated only at nadir, and they were obtained using the Leinonen B p2 R-G scattering model. The high-frequency channel footprint size of 10 km (see Table 4) was considered; therefore, eight TB_{sim} obtained from CPR profiles have been averaged to roughly reproduce the nominal MWR footprint resolution.

Figure 12 shows the simulated TBs computed at nadir for three of the four channels in the 325.15 GHz water vapor absorption band (325.15 ± 6.6, 325.15 ± 4.1, and 325.15 ± 1.2 GHz, in b, d, and f) and for the corresponding coupled channels in the 183.31 GHz band (178.31, 181.31, and 182.31 GHz in c, e, and g) (as shown previously in Figure 1). The TBs for the 176.31 GHz channel (Figure 12a) is also shown for comparison (this channel is expected to have similar behavior to the MHS 190 GHz channel shown in Figure 10c). The curves in each plot are obtained by varying the position of the SLW layer and these are compared to the clear-sky TBs and the TBs with no added SWL layer. Although the weighting functions of each pair of coupled channels in clear-sky conditions are equivalent (see the "Clear Sky" green dotted line for each row), the TB depression observed for each channel at 325.15 GHz band is much deeper than that observed for the corresponding channel at 183.31 GHz. The TB depression (scattering effect) increases moving from the inner channel (325.15 ± 1.2 GHz) to the outer channel (325.15 ± 6.6 GHz) in the absorption band. For these channels (with weighting function peaking lower in the atmosphere), a slight influence of the two higher SLW layers is also visible. It is possible to observe that the TB increase linked to the added SLW layers at 325.15 ± 6.6 GHz is similar to that at 176.31 GHz (≈+10 K) and higher than the corresponding coupled channel at 178.31 GHz (≈+6 K). However, by comparing the TB depression due to the snow/ice scattering, which is much higher at 325.15 ± 6.6 GHz (≈−40 K, max −50 K) than at 176.31 GHz (≈max −40 K) or at 178.31 GHz (max −20 K), it is evident that the SLW influence has a limited impact in masking the snowfall signal at 325.15 GHz. A similar analysis can be done for the coupled channels in the third row, where the impact of the SLW water layer is even more limited. Concerning the innermost channels (Figure 12f,g) the presence of the SLW layer does not show any influence. Also for these channels, the TB depression is much more evident for the 325.15 GHz channels than for the corresponding 183.31 GHz channel. It is worth noting that the 325.15 ± 6.6 and the 325.15 ± 4.1 GHz TB_{sim} also show a significant TB dip in the cloud anvil, demonstrating the high sensitivity to very low IWC values (see Figure 8). The innermost channel at 325.15 GHz (fourth row) also shows a high sensitivity to the IWC found at a higher altitude (at 47 °N, see Figure 6). It is possible to observe that the TB decrease due to the scattering from ice is much larger than the TB increase due the emission from the SLW layers. Moreover, while the TB increase due to the emission in the coupled channels is quite similar in terms of absolute values, the TB decrease due to the scattering is much larger at 325.15 GHz than at 183.31 GHz. Therefore, the differences between the coupled channels can be a very useful tool to investigate the ice signal independently from the presence of SLW layers.

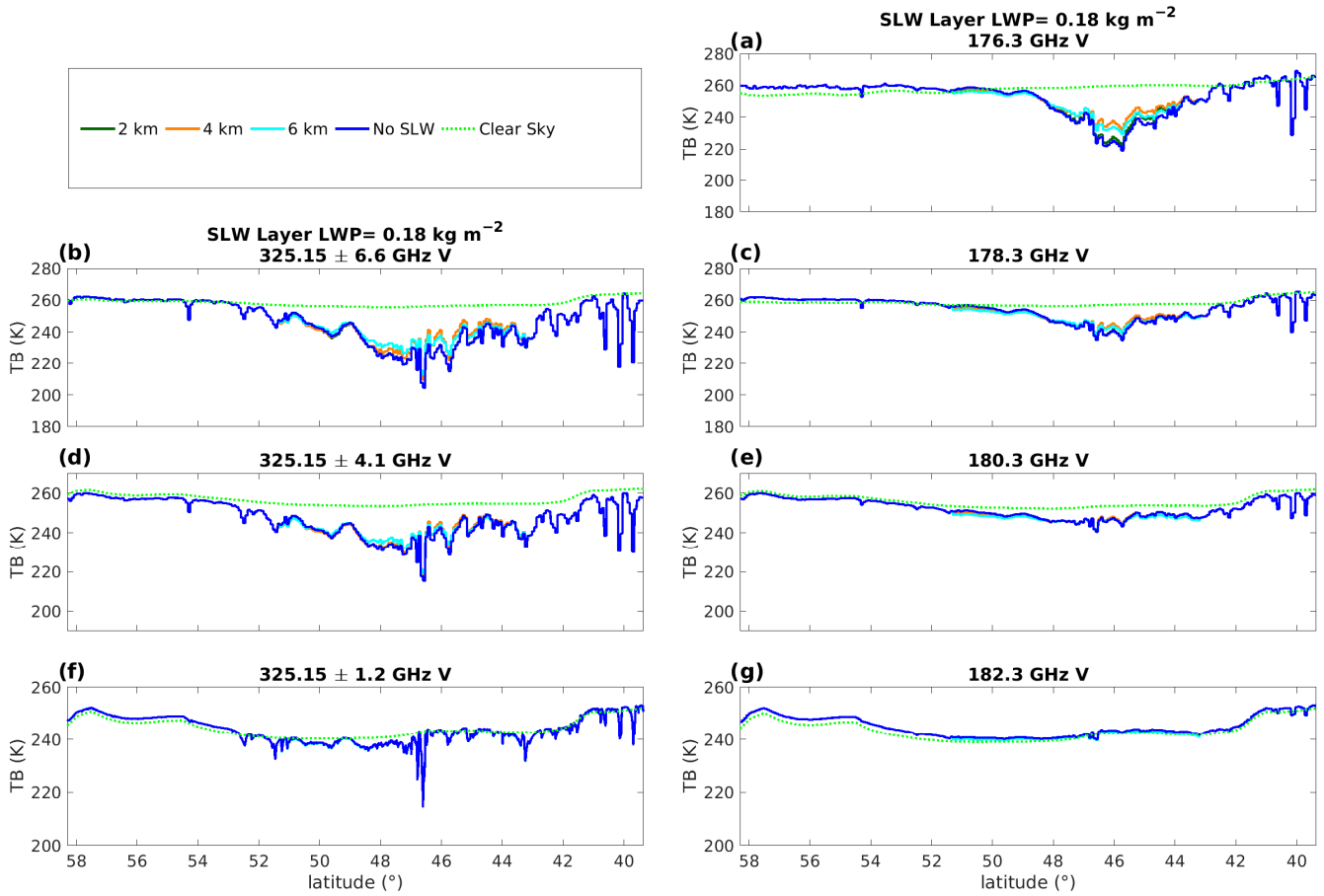


Figure 12. Case Study off Newfoundland: MWR TBs for three 325.15 GHz channels (**b**,**d**,**f**) and corresponding coupled channels at 183.31 GHz (**c**,**e**,**g**). TBs at 176.3 GHz are also shown (**a**). TBs were obtained with the R-G model leinonen B p2 and by adding a SLW layer to the CAPTIVATE-retrieved scene for a total LWP = 0.18 kg m^{-2}. Three different SLW layers at 2 km, 4 km—which roughly corresponds to the 253 K isotherm—and 6 km—which roughly corresponds to the 243 K isotherm—are considered. See Figure 9d for CPR reflectivity and SLW layers height, and Figure 9f for IWP/LWP values.

The sensitivity to the snowflake scattering signal was analyzed also by considering other R-G models. The analysis was carried out without adding the SLW layer to the scene because of its low impact on the TBs at these frequencies. In Figure 13, a comparison between simulated signals obtained by applying several R-G scattering models is reported for three channels of the 325.15 GHz water vapor absorption band. All simulations show a sensitivity to the presence of ice in the atmosphere, while the emission signal produced by the CAPTIVATE SLW is almost absent; in particular, in the shallow cloud system in the northern part of the event. The TB decrease due to scattering is less intense from the external to the internal channels; however, it is worth noting that the TB_{sim} obtained by applying two R-G models (koln-2017 and leinonen C) are very different from the others, showing no scattering effect also in the deeper part of the cloud.

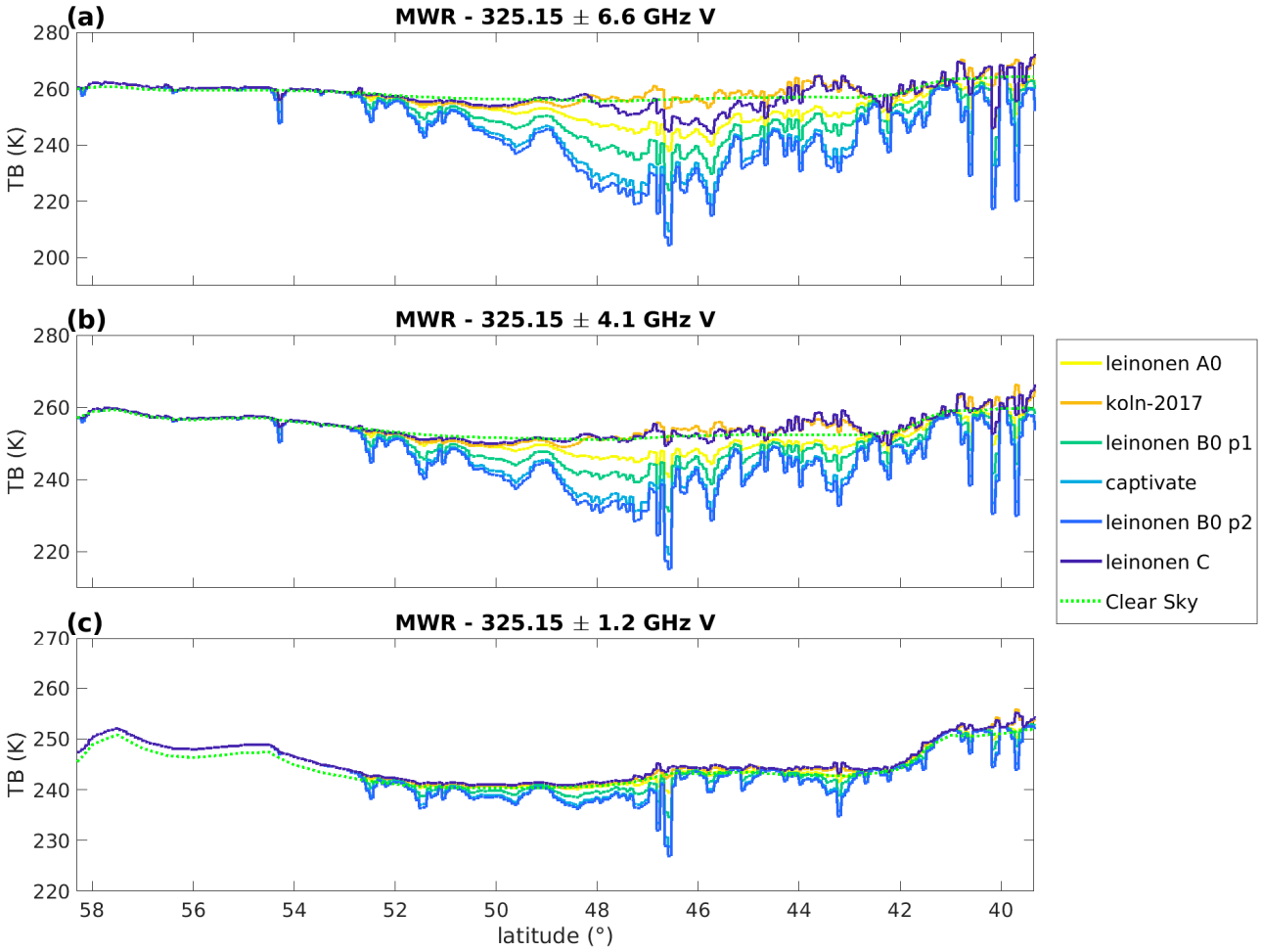


Figure 13. Comparison between the AWS-MWR TB_{sim} obtained by using several R-G models for 325.15 ± 6.6 GHz (**a**), 325.15 ± 4.1 (**b**), and 325.15 ± 1.2 GHz (**c**) channels. The green dotted line represents the TB_{CS}. See Figure 7 for CPR reflectivity, SLW position, and IWP/LWP values.

The analysis of the sensitivity to the snowflake scattering signal of the AWS-MWR 325.15 GHz channels was carried out not only for the case study, but also for an extended simulated dataset based on the same CPR/CALIOP observations of the 94 GHz TB dataset described in Section 2.6. Figure 14 shows the mean differences between the TB_{sim} of the coupled channels of the two vapor absorption bands as a function of IWP. In clear-sky conditions, the mean ΔTB is close to zero for all the R-G models. However, for IWP > 0 kg m^{-2}, the R-G models show different behaviors. The leinonen A0, leinonen B0 (p1 and p2), and captivate models show positive values that are proportional to the IWP value, indicating that the scattering effect due to the ice hydrometeors is significantly stronger in the 325.15 GHz channels than at the corresponding coupled channel in the 183.31 GHz band. For the external channel (325.15 ± 6.6 GHz), this effect is visible also for very low IWP (<1 kg m^{-2}), showing its high sensitivity to very light snowfall. On the other hand, the koln-2017 and leinonen C models show negative differences, and lack a well-defined trend in relation to IWP values, similarly to what has been shown in Figure 13. The combination of the 325.15 GHz TBs and radar-derived snowfall profiles can be exploited to retrieve information about the snowflake microphysics, which the different scattering models represent.

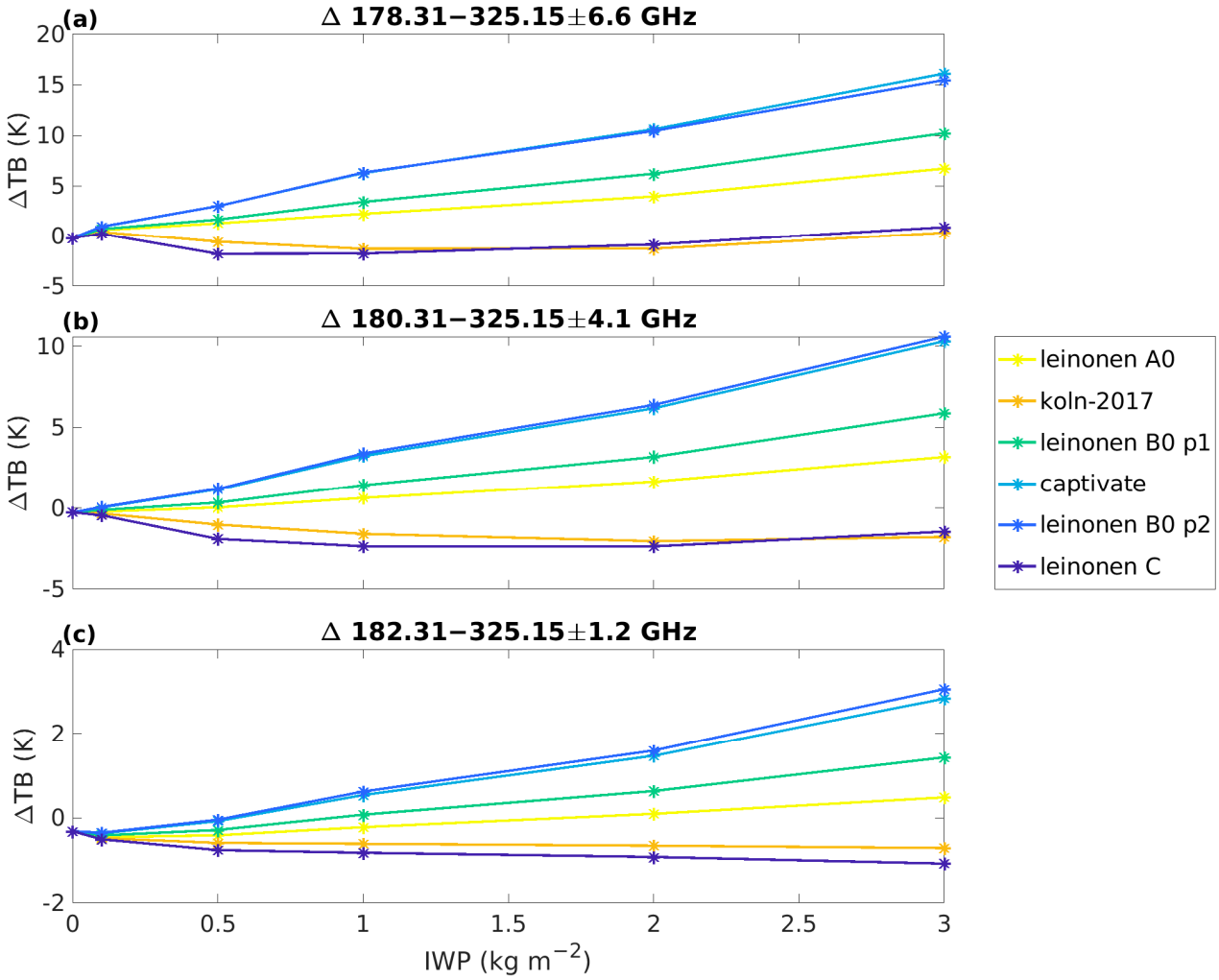


Figure 14. Differences between TB_{sim} for the coupled channels (see Section 2.6) in the two water vapor absorption bands obtained using six different R-G models.

4. Summary and Conclusions

The recent advancements in multi-channel passive microwave snowfall retrieval based on machine learning techniques trained by spaceborne cloud radar/lidar (CloudSat CPR/CALIOP) observational datasets look very promising. However, the detection of SLW layers embedded in snowing precipitating systems by combined radar/lidar spaceborne systems (including those on board the EarthCARE satellite) remains a fundamental observational gap. Depending on the frequency, the emission signal (TB warming) of SLW layers can partially or totally mask the snowfall scattering signal (TB cooling). The recent launch of the AWS, and its possible future operation with the EPS-Sterna constellation mission, offers new opportunities for snowfall global monitoring thanks to the availability of the MWR sub-mm channels (325.15 GHz) which are very sensitive to the presence of ice hydrometeors in the cloud. This study illustrates in detail the challenges in satellite MW-based monitoring and quantitative estimation of snowfall at higher latitudes linked to the presence of SLW, and how these challenges might be overcome through the exploitation of the AWS.

A cloud-radiation dataset built from CloudSat/CALIPSO snowfall observations coupled with a passive MW RTM was used in this study to simulate multi-channel TBs to be compared with available measurements. Cloud ice and liquid water content profiles retrieved by CAPTIVATE, a state-of-the-art retrieval algorithm used for the EarthCARE mission, applied to the suite of A-Train observations were used as input. Six different

scattering models were considered to try to reproduce the natural variability of the ice microphysics in snowfall conditions, while different scenarios of embedded SLW layers are considered to analyze the impact of SLW on the RTM simulations.

First, a closure radiative transfer study was performed between the TBs provided by the CloudSat passive mode (2B-94TB product) and the simulated TBs at 94 GHz. The results show large discrepancies in the presence of snow precipitating systems, especially in presence of deep clouds characterized by high IWP values. While the simulated TBs show the cooling effect due to the presence of high IWP, this behavior is not observed in the 2B-94TB product. This difference can be attributed to the missed detection of SLW, since if the analysis is limited only to observations where CAPTIVATE detects SLW, and consequently the SLW emission signal is reproduced by the RTM simulations, the simulated TBs show similar behavior to the 2B-94TB product.

This hypothesis has been verified by analyzing an oceanic snowfall case study off the island of Newfoundland, when a nearly coincident overpass by CloudSat/CALIPSO and the AMSU-A/MHS is available. Here, neither the MHS 89 GHz channel nor the 2B-94TB show any TB depression in the deeper part of the cloud, where SLW is not detected, while all simulations obtained with the different scattering models show a marked TB cooling. By adding a SLW layer embedded in the cloud, a better agreement with the multi-channel measured TBs is obtained. The comparison with the AMSU-A and MHS measurements show that the addition a SLW layer improves the agreement between simulated and observed TBs at low and high frequency. Moreover, a sensitivity study has been carried out by alternately varying the LWP and the height of the SLW layer embedded in the cloud; this analysis shows that lower frequency channels (50.3, 89/94 GHz) are very sensitive to LWP while the higher frequencies (especially between 157 and 165 GHz) are more sensitive to the SLW layer height. Similar behavior is obtained for the AWS-MWR channels in common with AMSU-A/MHS.

Finally, the simulation of the newly available AWS-MWR 325.15 GHz channels shows a much higher sensitivity to snowfall, with a much lower impact of the SLW layers on the scattering signal.

This study suggests that the AWS-MWR channels have the potential to be used not only for improving snowfall monitoring at higher latitudes, but also for cloud liquid and ice microphysics characterization. In particular:

1. The identification of the scattering regime of the ice cloud by exploiting mainly the new channels in the flanks of the 325.15 GHz line;
2. The detection of SLW layers (even when they are embedded in the cloud), by combining the use of low- and high-frequency channels;
3. The estimate of the cloud LWP (including the SLW), by exploiting the 50 GHz and 89 GHz channels;
4. The estimate of the SLW layers height by combining observations at 89 and 165.5 GHz with the five channels in the 183.31 GHz water vapor absorption band.

The availability of both AWS-MWR and EarthCARE observations in the near future will allow the creation of a PMW and radar/lidar coincidence dataset. This dataset, associated with the EarthCARE CPR passive mode, will be used to verify the actual AWS-MWR channels sensitivity to the SLW layers embedded in the cloud (which are not detected by active measuring systems). A proper verification of a mass estimate or even detection of these layers is, however, problematic with radar/lidar satellite products, and should be based on airborne measurements or ground-based remote sensing observations. Several airborne observation campaigns, such as the 2004 Mixed-Phase Arctic Cloud Experiment (M-PACE, [81]), the 2018 Southern Ocean Cloud Radiation and Aerosol Transport Experimental Study (SOCRATES, [82]), the Investigation of Microphysics and Precipitation for Atlantic Coast-Threatening Snowstorms (IMPACTS) Campaign [83], and the airborne campaigns part of the AC3 project [84,85], can be used as references for future studies. The same dataset will be exploited to develop an ML-based snowfall algorithm for AWS, with a similar approach to that used for the ATMS snowfall retrieval algorithm, SLALOM-CT

(see Ref. [54]). Moreover, the synergy between AWS-MWR and EarthCARE missions will allow the analysis of snowfall phenomena with an unprecedented level of accuracy by simultaneously characterizing the snowfall intensity, cloud ice scattering properties, and the SLW layers. Therefore, the development of a snowfall retrieval algorithm, based on EarthCARE and AWS-MWR combined observations, possibly using the optimal estimation approach, will be a future development of this study, with possible future applications for the EPS-Sterna constellation. Finally, the availability of unprecedented high spatial resolution of CIMR MW measurements at low frequency (about 5 km at 37 GHz) would certainly offer new insights for the characterization of the complex and variable surface conditions at high latitudes (sea ice, coastlines, water bodies, snow), which have not been considered in this study, and could be used as auxiliary information in the AWS-based precipitation retrievals.

Author Contributions: Conceptualization: A.C. and D.C.; methodology, A.C., P.S., D.C. and G.P.; software, A.C. and A.B.; formal analysis, A.C. and D.C.; investigation, A.C., P.S., D.C., G.P. and A.B.; resources, A.B.; data curation, A.C., P.S., D.C., G.P. and A.B.; writing—original draft preparation, A.C.; writing—review and editing, A.C., P.S., D.C., G.P. and A.B.; visualization, A.C. and D.C.; supervision, project administration, funding acquisition, G.P. and A.B. All authors have read and agreed to the published version of the manuscript.

Funding: This research has been supported by the European Space Agency (ESA) under the RAINCAST project Contract Continuation Notice 2 (ESA Contract number: ESA AO/1-9324/18/NL/NA).

Data Availability Statement: The raw data supporting the conclusions of this article will be made available by the authors on request.

Acknowledgments: Many thanks to Ben Courtier (University of Leicester) and Shannon Mason (ECMWF) for providing the CAPTIVATE retrieval outputs.

Conflicts of Interest: The authors declare no conflicts of interest.

List of Acronyms

AMSR-E	Advanced Microwave Scanning Radiometer for EOS
AMSU-A	Atmospheric Measurement Sounding Unit-A
ATLID	Atmospheric Lidar
ATMS	Advanced Technology Microwave Sounder
AWS	Arctic Weather Satellite
CALIOP	Cloud-Aerosol Lidar with Orthogonal Polarization
CALIPSO	Cloud-Aerosol Lidar and Infrared Pathfinder Satellite Observations
CAPTIVATE	Cloud and precipitation profiles derived from the algorithm developed for the EarthCARE mission
CIMR	Copernicus Imaging Microwave Radiometer
CPR	Cloud Profiling Radar
DARDAR	raDAR/liDAR
DPR	Dual-frequency Precipitation Radar
ECMWF	European Centre for Medium Range Forecast
EarthCARE	Earth Cloud Aerosol and Radiation Explorer
EPS-Sterna	EUMETSAT Polar System Sterna
ESA	European Space Agency
EUMETSAT	European Organisation for the Exploitation of Meteorological Satellites
GPM	Global Precipitation Measurement
GPM-CO	Global Precipitation Measurement- Core Observatory
IFOV	instantaneous field of view
IWC	Ice Water Content
IWP	Ice Water Path
JAXA	Japan Aerospace eXploration Agency
LEO	Low Earth Orbit
LWC	Liquid Water Content

LWP	Liquid Water Path
MLMHS	Machine LearningMicrowave Humidity Sounder
MSI	Multi-Spectral Imager
MW	Microwave
MWR	Microwave Radiometer
NASA	National Aeronautics and Space Administration
NEΔT	noise equivalent delta temperature
PMW	Passive Microwave
PSD	particle size distributions
R-G	Rayleigh-Gans
RTM	radiative transfer model
RWC	Rain Water Content
SLALOM	Snow retrievaL ALgorithm fOr gMi
SLALOM-CT	Snow retrievaL ALgorithm fOr gpM-Cross Track
SLW	Supercooled Liquid Water
SLWP	Supercooled Liquid Water Path
T_{2m}	2m Temperature
TB	Brightness Temperature
TB_{CS}	clear-sky simulated TBs
TB_{obs}	observed TBs
TB_{sim}	simulated TBs
TPW	Total Precipitable Water
WIVERN	Wind VElocity Radar Nephoscope

References

1. Liu, G.; Seo, E. Detecting Snowfall over Land by Satellite High-frequency Microwave Observations: The Lack of Scattering Signature and a Statistical Approach. *J. Geophys. Res. Atmos.* **2013**, *118*, 1376–1387. [CrossRef]
2. Bintanja, R.; Selten, F.M. Future Increases in Arctic Precipitation Linked to Local Evaporation and Sea-Ice Retreat. *Nature* **2014**, *509*, 479–482. [CrossRef] [PubMed]
3. Vihma, T.; Screen, J.; Tjernström, M.; Newton, B.; Zhang, X.; Popova, V.; Deser, C.; Holland, M.; Prowse, T. The Atmospheric Role in the Arctic Water Cycle: A Review on Processes, Past and Future Changes, and Their Impacts. *J. Geophys. Res. Biogeosciences* **2016**, *121*, 586–620. [CrossRef]
4. Panegrossi, G.; Casella, D.; Sanò, P.; Camplani, A.; Battaglia, A. Chapter 12—Recent Advances and Challenges in Satellite-Based Snowfall Detection and Estimation. In *Precipitation Science*; Michaelides, S., Ed.; Elsevier: Amsterdam, The Netherlands, 2022; pp. 333–376, ISBN 978-0-12-822973-6.
5. Stephens, G.L.; Vane, D.G.; Boain, R.J.; Mace, G.G.; Sassen, K.; Wang, Z.; Illingworth, A.J.; O'connor, E.J.; Rossow, W.B.; Durden, S.L.; et al. THE CLOUDSAT MISSION AND THE A-TRAIN. *Bull. Am. Meteorol. Soc.* **2002**, *83*, 1771–1790. [CrossRef]
6. Illingworth, A.J.; Barker, H.W.; Beljaars, A.; Ceccaldi, M.; Chepfer, H.; Clerbaux, N.; Cole, J.; Delanoë, J.; Domenech, C.; Donovan, D.P.; et al. The Earthcare Satellite: The next Step Forward in Global Measurements of Clouds, Aerosols, Precipitation, and Radiation. *Bull. Am. Meteorol. Soc.* **2015**, *96*, 1311–1332. [CrossRef]
7. Illingworth, A.J.; Battaglia, A.; Bradford, J.; Forsythe, M.; Joe, P.; Kollias, P.; Lean, K.; Lori, M.; Mahfouf, J.F.; Melo, S.; et al. A New Satellite Concept to Provide Global In-Cloud Winds, Precipitation, and Cloud Properties. *Bull. Am. Meteorol. Soc.* **2018**, *99*, 1669–1687. [CrossRef]
8. Kulie, M.S.; Milani, L.; Wood, N.B.; Tushaus, S.A.; Bennartz, R.; L'Ecuyer, T.S. A Shallow Cumuliform Snowfall Census Using Spaceborne Radar. *J. Hydrometeorol.* **2016**, *17*, 1261–1279. [CrossRef]
9. Milani, L.; Kulie, M.S.; Casella, D.; Dietrich, S.; L'Ecuyer, T.S.; Panegrossi, G.; Porcù, F.; Sanò, P.; Wood, N.B. CloudSat Snowfall Estimates over Antarctica and the Southern Ocean: An Assessment of Independent Retrieval Methodologies and Multi-Year Snowfall Analysis. *Atmos. Res.* **2018**, *213*, 121–135. [CrossRef]
10. Behrangi, A.; Christensen, M.; Richardson, M.; Lebsock, M.; Stephens, G.; Huffman, G.J.; Bolvin, D.; Adler, R.F.; Gardner, A.; Lambrigtsen, B.; et al. Status of High-latitude Precipitation Estimates from Observations and Reanalyses. *J. Geophys. Res. Atmos.* **2016**, *121*, 4468–4486. [CrossRef]
11. Mroz, K.; Montopoli, M.; Battaglia, A.; Panegrossi, G.; Kirstetter, P.; Baldini, L. Cross Validation of Active and Passive Microwave Snowfall Products over the Continental United States. *J. Hydrometeorol.* **2021**, *22*, 1297–1315. [CrossRef]
12. Tang, G.; Wen, Y.; Gao, J.; Long, D.; Ma, Y.; Wan, W.; Hong, Y. Similarities and Differences between Three Coexisting Spaceborne Radars in Global Rainfall and Snowfall Estimation. *Water Resour. Res.* **2017**, *53*, 3835–3853. [CrossRef]
13. Battaglia, A.; Panegrossi, G. What Can We Learn from the Cloudsat Radiometric Mode Observations of Snowfall over the Ice-Free Ocean? *Remote Sens.* **2020**, *12*, 3285. [CrossRef]
14. Bennartz, R.; Fell, F.; Pettersen, C.; Shupe, M.D.; Schuettemeyer, D. Spatial and Temporal Variability of Snowfall over Greenland from CloudSat Observations. *Atmos. Chem. Phys.* **2019**, *19*, 8101–8121. [CrossRef]

15. Matrosov, S.Y. Comparative Evaluation of Snowfall Retrievals from the CloudSat W-Band Radar Using Ground-Based Weather Radars. *J. Atmos. Ocean. Technol.* **2019**, *36*, 101–111. [CrossRef]
16. Palerme, C.; Claud, C.; Wood, N.B.; L'Ecuyer, T.; Genthon, C. How Does Ground Clutter Affect CloudSat Snowfall Retrievals over Ice Sheets? *IEEE Geosci. Remote Sens. Lett.* **2019**, *16*, 342–346. [CrossRef]
17. Milani, L.; Wood, N.B. Biases in Cloudsat Falling Snow Estimates Resulting from Daylight-Only Operations. *Remote Sens.* **2021**, *13*, 2041. [CrossRef]
18. Skofronick-Jackson, G.; Petersen, W.A.; Berg, W.; Kidd, C.; Stocker, E.F.; Kirschbaum, D.B.; Kakar, R.; Braun, S.A.; Huffman, G.J.; Iguchi, T.; et al. The Global Precipitation Measurement (GPM) Mission for Science and Society. *Bull. Am. Meteorol. Soc.* **2017**, *98*, 1679–1695. [CrossRef]
19. Casella, D.; Panegrossi, G.; Sanò, P.; Marra, A.C.; Dietrich, S.; Johnson, B.T.; Kulie, M.S. Evaluation of the GPM-DPR Snowfall Detection Capability: Comparison with CloudSat-CPR. *Atmos. Res.* **2017**, *197*, 64–75. [CrossRef]
20. Scarsi, F.E.; Battaglia, A.; Maahn, M.; Lhermitte, S. How to Reduce Sampling Errors in Spaceborne Cloud Radar-Based Snowfall Estimates. *Atm. Meas. Tech. Disc* **2024**. [CrossRef]
21. Kidd, C.; Huffman, G. Global Precipitation Measurement. *Meteorol. Appl.* **2011**, *18*, 334–353. [CrossRef]
22. Levizzani, V.; Laviola, S.; Cattani, E. Detection and Measurement of Snowfall from Space. *Remote Sens.* **2011**, *3*, 145–166. [CrossRef]
23. Bennartz, R.; Bauer, P. Sensitivity of Microwave Radiances at 85-183 GHz to Precipitating Ice Particles. *Radio Sci.* **2003**, *38*, 40. [CrossRef]
24. Skofronick-Jackson, G.; Johnson, B.T. Surface and Atmospheric Contributions to Passive Microwave Brightness Temperatures for Falling Snow Events. *J. Geophys. Res. Atmos.* **2011**, *116*. [CrossRef]
25. Eriksson, P.; Jamali, M.; Mendrok, J.; Buehler, S.A. On the Microwave Optical Properties of Randomly Oriented Ice Hydrometeors. *Atmos. Meas. Tech.* **2015**, *8*, 1913–1933. [CrossRef]
26. Ebtehaj, A.M.; Kummerow, C.D. Microwave Retrievals of Terrestrial Precipitation over Snow-covered Surfaces: A Lesson from the GPM Satellite. *Geophys. Res. Lett.* **2017**, *44*, 6154–6162. [CrossRef]
27. Panegrossi, G.; Rysman, J.-F.; Casella, D.; Marra, A.; Sanò, P.; Kulie, M. CloudSat-Based Assessment of GPM Microwave Imager Snowfall Observation Capabilities. *Remote Sens.* **2017**, *9*, 1263. [CrossRef]
28. Takbiri, Z.; Ebtehaj, A.; Foufoula-Georgiou, E.; Kirstetter, P.E.; Turk, F.J. A Prognostic Nested K-Nearest Approach for Microwave Precipitation Phase Detection over Snow Cover. *J. Hydrometeorol.* **2019**, *20*, 251–274. [CrossRef]
29. You, Y.; Wang, N.Y.; Ferraro, R.; Rudlosky, S. Quantifying the Snowfall Detection Performance of the GPM Microwave Imager Channels over Land. *J. Hydrometeorol.* **2017**, *18*, 729–751. [CrossRef]
30. Kongoli, C.; Meng, H.; Dong, J.; Ferraro, R. A Snowfall Detection Algorithm over Land Utilizing High-Frequency Passive Microwave Measurements—Application to ATMS. *J. Geophys. Res.* **2015**, *120*, 1918–1932. [CrossRef]
31. Camplani, A.; Casella, D.; Sanò, P.; Panegrossi, G. The Passive Microwave Empirical Cold Surface Classification Algorithm (PESCA): Application to GMI and ATMS. *J. Hydrometeorol.* **2021**, *22*, 1727–1744. [CrossRef]
32. Kulie, M.S.; Bennartz, R.; Greenwald, T.J.; Chen, Y.; Weng, F. Uncertainties in Microwave Properties of Frozen Precipitation: Implications for Remote Sensing and Data Assimilation. *J. Atmos. Sci.* **2010**, *67*, 3471–3487. [CrossRef]
33. Kuo, K.S.; Olson, W.S.; Johnson, B.T.; Grecu, M.; Tian, L.; Clune, T.L.; Van Aartsen, B.H.; Heymsfield, A.J.; Liao, L.; Meneghini, R. Full Access the Microwave Radiative Properties of Falling Snow Derived from Nonspherical Ice Particle Models. Part I: An Extensive Database of Simulated Pristine Crystals and Aggregate Particles, and Their Scattering Properties. *J. Appl. Meteorol. Climatol.* **2016**, *55*, 691–708. [CrossRef]
34. Ekelund, R.; Eriksson, P. Impact of Ice Aggregate Parameters on Microwave and Sub-Millimetre Scattering Properties. *J. Quant. Spectrosc. Radiat. Transf.* **2019**, *224*, 233–246. [CrossRef]
35. Munchak, S.J.; Ringerud, S.; Brucker, L.; You, Y.; De Gelis, I.; Prigent, C. An Active-Passive Microwave Land Surface Database from GPM. *IEEE Trans. Geosci. Remote Sens.* **2020**, *58*, 6224–6242. [CrossRef]
36. Prigent, C.; Aires, F.; Rossow, W.B. Land Surface Microwave Emissivities over the Globe for a Decade. *Bull. Am. Meteorol. Soc.* **2006**, *87*, 1573–1584. [CrossRef]
37. Turk, F.J.; Ringerud, S.E.; You, Y.; Camplani, A.; Casella, D.; Panegrossi, G.; Sanò, P.; Ebtehaj, A.; Guilloteau, C.; Utsumi, N.; et al. Adapting Passive Microwave-Based Precipitation Algorithms to Variable Microwave Land Surface Emissivity to Improve Precipitation Estimation from the GPM Constellation. *J. Hydrometeorol.* **2021**, *22*, 1755–1781. [CrossRef]
38. Johnson, B.T.; Olson, W.S.; Skofronick-Jackson, G. The Microwave Properties of Simulated Melting Precipitation Particles: Sensitivity to Initial Melting. *Atmos. Meas. Tech.* **2016**, *9*, 9–21. [CrossRef]
39. Kneifel, S.; Leinonen, J.; Tyynelä, J.; Ori, D.; Battaglia, A.; Kneifel, S.; Ori, D.; Leinonen, J.; Tyynelä, J. Scattering of Hydrometeors. In *Advances in Global Change Research*; Springer: Cham, Switzerland, 2020; Volume 67, pp. 249–276.
40. Turk, F.J.; Ringerud, S.E.; Camplani, A.; Casella, D.; Chase, R.J.; Ebtehaj, A.; Gong, J.; Kulie, M.; Liu, G.; Milani, L.; et al. Applications of a Cloudsat-Trmm and Cloudsat-Gpm Satellite Coincidence Dataset. *Remote Sens.* **2021**, *13*, 2264. [CrossRef]
41. Korolev, A.V.; Isaac, G.A.; Cober, S.G.; Strapp, J.W.; Hallett, J. Microphysical Characterization of Mixed-Phase Clouds. *Q. J. R. Meteorol. Soc.* **2003**, *129*, 39–65. [CrossRef]
42. Maciel, F.V.; Diao, M.; Yang, C.A. Partition between Supercooled Liquid Droplets and Ice Crystals in Mixed-Phase Clouds Based on Airborne in Situ Observations. *Atmos. Meas. Tech.* **2024**, *17*, 4843–4861. [CrossRef]

43. Ricaud, P.; Del Guasta, M.; Lupi, A.; Roehrig, R.; Bazile, E.; Durand, P.; Attié, J.L.; Nicosia, A.; Grigioni, P. Supercooled Liquid Water Clouds Observed over Dome C, Antarctica: Temperature Sensitivity and Cloud Radiative Forcing. *Atmos. Chem. Phys.* **2024**, *24*, 613–630. [CrossRef]
44. Wang, Y.; Liu, G.; Seo, E.K.; Fu, Y. Liquid Water in Snowing Clouds: Implications for Satellite Remote Sensing of Snowfall. *Atmos. Res.* **2013**, *131*, 60–72. [CrossRef]
45. Battaglia, A.; Delanoë, J. Synergies and Complementarities of CloudSat-CALIPSO Snow Observations. *J. Geophys. Res. Atmos.* **2013**, *118*, 721–731. [CrossRef]
46. Hogan, R.J.; Francis, P.N.; Flentje, H.; Illingworth, A.J.; Quante, M.; Pelon, J. Characteristics of Mixed-Phase Clouds. I: Lidar, Radar and Aircraft Observations from CLARE'98. *Q. J. R. Meteorol. Soc.* **2003**, *129*, 2089–2116. [CrossRef]
47. Ceccaldi, M.; Delanoë, J.; Hogan, R.J.; Pounder, N.L.; Protat, A.; Pelon, J. From CloudSat-CALIPSO to EarthCare: Evolution of the DARDAR Cloud Classification and Its Comparison to Airborne Radar-Lidar Observations. *J. Geophys. Res. Atmos.* **2013**, *118*, 7962–7981. [CrossRef]
48. Listowski, C.; Delanoë, J.; Kirchgaessner, A.; Lachlan-Cope, T.; King, J. Antarctic Clouds, Supercooled Liquid Water and Mixed Phase, Investigated with DARDAR: Geographical and Seasonal Variations. *Atmos. Chem. Phys.* **2019**, *19*, 6771–6808. [CrossRef]
49. Edel, L.; Rysman, J.F.; Claud, C.; Palerme, C.; Genthon, C. Potential of Passive Microwave around 183 GHz for Snowfall Detection in the Arctic. *Remote Sens.* **2019**, *11*, 2200. [CrossRef]
50. Adhikari, A.; Ehsani, M.R.; Song, Y.; Behrangi, A. Comparative Assessment of Snowfall Retrieval From Microwave Humidity Sounders Using Machine Learning Methods. *Earth Sp. Sci.* **2020**, *7*, e2020EA001357. [CrossRef]
51. Meng, H.; Dong, J.; Ferraro, R.; Yan, B.; Zhao, L.; Kongoli, C.; Wang, N.Y.; Zavodsky, B. A 1DVAR-Based Snowfall Rate Retrieval Algorithm for Passive Microwave Radiometers. *J. Geophys. Res.* **2017**, *122*, 6520–6540. [CrossRef]
52. Rysman, J.F.; Panegrossi, G.; Sanò, P.; Marra, A.C.; Dietrich, S.; Milani, L.; Kulie, M.S. SLALOM: An All-Surface Snow Water Path Retrieval Algorithm for the GPM Microwave Imager. *Remote Sens.* **2018**, *10*, 1278. [CrossRef]
53. Rysman, J.F.; Panegrossi, G.; Sanò, P.; Marra, A.C.; Dietrich, S.; Milani, L.; Kulie, M.S.; Casella, D.; Camplani, A.; Claud, C.; et al. Retrieving Surface Snowfall With the GPM Microwave Imager: A New Module for the SLALOM Algorithm. *Geophys. Res. Lett.* **2019**, *46*, 13593–13601. [CrossRef]
54. Sanò, P.; Casella, D.; Camplani, A.; D'adderio, L.P.; Panegrossi, G. A Machine Learning Snowfall Retrieval Algorithm for ATMS. *Remote Sens.* **2022**, *14*, 1467. [CrossRef]
55. Camplani, A.; Casella, D.; Sanò, P.; Panegrossi, G. The High LAtitude SNowfall Detection and Estimation ALgorithm for ATMS (HANDEL-ATMS): A New Algorithm for Snowfall Retrieval at High Latitudes. *Atmos. Meas. Tech.* **2024**, *17*, 2195–2217. [CrossRef]
56. Delanoë, J.; Hogan, R.J. Combined CloudSat-CALIPSO-MODIS Retrievals of the Properties of Ice Clouds. *J. Geophys. Res. Atmos.* **2010**, *115*. [CrossRef]
57. Mason, S.L.; Hogan, R.J.; Bozzo, A.; Pounder, N.L. A Unified Synergistic Retrieval of Clouds, Aerosols, and Precipitation from EarthCARE: The ACM-CAP Product. *Atmos. Meas. Tech.* **2023**, *16*, 3459–3486. [CrossRef]
58. Winker, D.M.; Pelon, J.R.; McCormick, M.P. CALIPSO Mission: Spaceborne Lidar for Observation of Aerosols and Clouds. In *Proceedings of the Lidar Remote Sensing for Industry and Environment Monitoring III*; SPIE: Bellingham, WA, USA, 2003; Volume 4893, pp. 1–11.
59. Winker, D.M.; Pelon, J.; Coakley, J.A.; Ackerman, S.A.; Charlson, R.J.; Colarco, P.R.; Flamant, P.; Fu, Q.; Hoff, R.M.; Kittaka, C.; et al. The CALIPSO Mission. *Bull. Am. Meteorol. Soc.* **2010**, *91*, 1211–1230. [CrossRef]
60. Mace, G.G.; Avey, S.; Cooper, S.; Lebsock, M.; Tanelli, S.; Dobrowalski, G. Retrieving Co-Occurring Cloud and Precipitation Properties of Warm Marine Boundary Layer Clouds with A-Train Data. *J. Geophys. Res.* **2016**, *121*, 4008–4033. [CrossRef]
61. Lebsock, M.D.; Suzuki, K. Uncertainty Characteristics of Total Water Path Retrievals in Shallow Cumulus Derived from Spaceborne Radar/Radiometer Integral Constraints. *J. Atmos. Ocean. Technol.* **2016**, *33*, 1597–1609. [CrossRef]
62. Mason, S.L.; Chiu, J.C.; Hogan, R.J.; Tian, L. Improved Rain Rate and Drop Size Retrievals from Airborne Doppler Radar. *Atmos. Chem. Phys.* **2017**, *17*, 11567–11589. [CrossRef]
63. Mason, S.L.; Chiu, C.J.; Hogan, R.J.; Moisseev, D.; Kneifel, S. Retrievals of Riming and Snow Density From Vertically Pointing Doppler Radars. *J. Geophys. Res. Atmos.* **2018**, *123*, 13,807–13,834. [CrossRef]
64. Courtier, B.; Mason, L.; Shannon; Hogan, R. Synergistic CloudSat-CALIPSO-MODIS Retrievals of Cloud-Aerosol-Precipitation (CCM-CAP) 2024. Available online: https://catalogue.ceda.ac.uk/uuid/abe7ca8911a94147888b2859501d4caa/ (accessed on 29 October 2024).
65. Kummerow, C. On the Accuracy of the Eddington Approximation for Radiative Transfer in the Microwave Frequencies. *J. Geophys. Res. Atmos.* **1993**, *98*, 2757–2765. [CrossRef]
66. Ulaby, F.T.; Long, D.J.; Blackwell, W.J.; Elachi, C.; Fung, A.K.; Ruf, C.; Sarabandi, K.; Zebker, H.A.; Van Zyl, J. *Microwave Radar and Radiometric Remote Sensing*, 4th ed.; University of Michigan Press: Ann Arbor, MI, USA, 2014; ISBN 978-0-472-11935-6.
67. Barlakas, V.; Galligani, V.S.; Geer, A.J.; Eriksson, P. On the Accuracy of RTTOV-SCATT for Radiative Transfer at All-Sky Microwave and Submillimeter Frequencies. *J. Quant. Spectrosc. Radiat. Transf.* **2022**, *283*, 108137. [CrossRef]
68. Rosenkranz, P.W. A Comparison of Measurements and Models Iv- v, I. *Radio Sci.* **1998**, *33*, 919–928. [CrossRef]
69. Partain, P. CloudSat ECMWF-AUX Auxiliary Data Product Process Description and Interface Control Document, Product Version P1_R05. Available online: https://www.cloudsat.cira.colostate.edu/cloudsat-static/info/dl/ecmwf-aux/ECMWF-AUX.PDICD.P1_R05.rev0.pdf (accessed on 29 October 2024).

70. Prigent, C.; Aires, F.; Wang, D.; Fox, S.; Harlow, C. Sea-surface Emissivity Parametrization from Microwaves to Millimetre Waves. *Q. J. R. Meteorol. Soc.* **2017**, *143*, 596–605. [CrossRef]
71. Turner, D.D.; Kneifel, S.; Cadeddu, M.P. An Improved Liquid Water Absorption Model at Microwave Frequencies for Supercooled Liquid Water Clouds. *J. Atmos. Ocean. Technol.* **2016**, *33*, 33–44. [CrossRef]
72. Tridon, F.; Battaglia, A.; Kneifel, S. Estimating Total Attenuation Using Rayleigh Targets at Cloud Top: Applications in Multilayer and Mixed-Phase Clouds Observed by Ground-Based Multifrequency Radars. *Atmos. Meas. Tech.* **2020**, *13*, 5065–5085. [CrossRef]
73. Leinonen, J.; Szyrmer, W. Radar Signatures of Snowflake Riming: A Modeling Study. *Earth Sp. Sci.* **2015**, *2*, 346–358. [CrossRef]
74. Leinonen, J.; Kneifel, S.; Hogan, R.J. Evaluation of the Rayleigh–Gans Approximation for Microwave Scattering by Rimed Snowflakes. *Q. J. R. Meteorol. Soc.* **2018**, *144*, 77–88. [CrossRef]
75. Hogan, R.J.; Westbrook, C.D. Equation for the Microwave Backscatter Cross Section of Aggregate Snowflakes Using the Self-Similar Rayleigh-Gans Approximation. *J. Atmos. Sci.* **2014**, *71*, 3292–3301. [CrossRef]
76. Hogan, R.J.; Honeyager, R.; Tyynelä, J.; Kneifel, S. Calculating the Millimetre-Wave Scattering Phase Function of Snowflakes Using the Self-Similar Rayleigh–Gans Approximation. *Q. J. R. Meteorol. Soc.* **2017**, *143*, 834–844. [CrossRef]
77. Tridon, F.; Battaglia, A.; Chase, R.J.; Turk, F.J.; Leinonen, J.; Kneifel, S.; Mroz, K.; Finlon, J.; Bansemer, A.; Tanelli, S.; et al. The Microphysics of Stratiform Precipitation During OLYMPEX: Compatibility Between Triple-Frequency Radar and Airborne In Situ Observations. *J. Geophys. Res. Atmos.* **2019**, *124*, 8764–8792. [CrossRef]
78. Brown, P.R.A.; Francis, P.N. Improved Measurements of the Ice Water Content in Cirrus Using a Total-Water Probe. *J. Atmos. Ocean. Technol.* **1995**, *12*, 410–414. [CrossRef]
79. Francis, P.N.; Hignett, P.; Macke, A. The Retrieval of Cirrus Cloud Properties from Aircraft Multi-spectral Reflectance Measurements during EUCREX'93. *Q. J. R. Meteorol. Soc.* **1998**, *124*, 1273–1291. [CrossRef]
80. Anderson, G.P.; Clough, S.A.; Kneizys, F.X.; Chetwynd, J.H.; Shettle, E.P. AFGL Atmospheric Constituent Profiles (0–120 Km). Available online: https://apps.dtic.mil/sti/tr/pdf/ADA175173.pdf (accessed on 29 October 2024).
81. Verlinde, J.; Harrington, J.Y.; McFarquhar, G.M.; Yannuzzi, V.T.; Avramov, A.; Greenberg, S.; Johnson, N.; Zhang, G.; Poellot, M.R.; Mather, J.H.; et al. The Mixed-Phase Arctic Cloud Experiment. *Bull. Am. Meteorol. Soc.* **2007**, *88*, 205–221. [CrossRef]
82. McFarquhar, G.M.; Bretherton, C.S.; Marchand, R.; Protat, A.; DeMott, P.J.; Alexander, S.P.; Roberts, G.C.; Twohy, C.H.; Toohey, D.; Siems, S.; et al. Observations of Clouds, Aerosols, Precipitation, and Surface Radiation over the Southern Ocean. *Bull. Am. Meteorol. Soc.* **2021**, *102*, E894–E928. [CrossRef]
83. McMurdie, L.A.; Heymsfield, G.M.; Yorks, J.E.; Braun, S.A.; Skofronick-Jackson, G.; Rauber, R.M.; Yuter, S.; Colle, B.; McFarquhar, G.M.; Poellot, M.; et al. Chasing Snowstorms: The Investigation of Microphysics and Precipitation for Atlantic Coast-Threatening Snowstorms (IMPACTS) Campaign. *Bull. Am. Meteorol. Soc.* **2022**, *103*, E1243–E1269. [CrossRef]
84. Griesche, H.J.; Seifert, P.; Engelmann, R.; Radenz, M.; Hofer, J.; Althausen, D.; Walbröl, A.; Barrientos-Velasco, C.; Baars, H.; Dahlke, S.; et al. Cloud Micro- and Macrophysical Properties from Ground-Based Remote Sensing during the MOSAiC Drift Experiment. *Sci. Data* **2024**, *11*, 505. [CrossRef]
85. Wendisch, M.; Crewell, S.; Ehrlich, A.; Herber, A.; Kirbus, B.; Lüpkes, C.; Mech, M.; Abel, S.J.; Akansu, E.F.; Ament, F.; et al. Overview: Quasi-Lagrangian Observations of Arctic Air Mass Transformations—Introduction and Initial Results of the HALO–(AC)3 Aircraft Campaign. *EGUsphere* **2024**, *24*, 8865–8892.

Disclaimer/Publisher's Note: The statements, opinions and data contained in all publications are solely those of the individual author(s) and contributor(s) and not of MDPI and/or the editor(s). MDPI and/or the editor(s) disclaim responsibility for any injury to people or property resulting from any ideas, methods, instructions or products referred to in the content.